

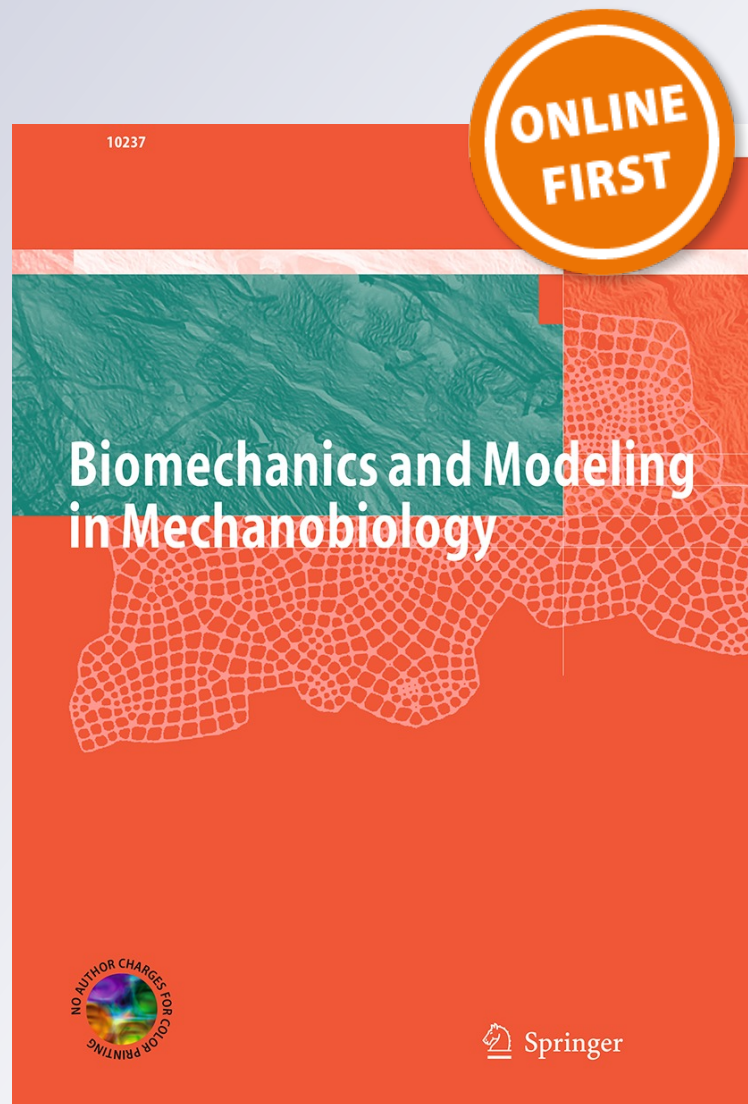
*Toward translating near-infrared spectroscopy oxygen saturation data for the non-invasive prediction of spatial and temporal hemodynamics during exercise*

**Laura Ellwein, Margaret M. Samyn, Michael Danduran, Sheila Schindler-Ivens, Stacy Liebham & John F. LaDisa**

**Biomechanics and Modeling in Mechanobiology**

ISSN 1617-7959

Biomech Model Mechanobiol  
DOI 10.1007/s10237-016-0803-4



**Your article is protected by copyright and all rights are held exclusively by Springer-Verlag Berlin Heidelberg. This e-offprint is for personal use only and shall not be self-archived in electronic repositories. If you wish to self-archive your article, please use the accepted manuscript version for posting on your own website. You may further deposit the accepted manuscript version in any repository, provided it is only made publicly available 12 months after official publication or later and provided acknowledgement is given to the original source of publication and a link is inserted to the published article on Springer's website. The link must be accompanied by the following text: "The final publication is available at [link.springer.com](http://link.springer.com)".**

# Toward translating near-infrared spectroscopy oxygen saturation data for the non-invasive prediction of spatial and temporal hemodynamics during exercise

Laura Ellwein<sup>1,2</sup> · Margaret M. Samyn<sup>1,3</sup> · Michael Danduran<sup>5</sup> ·  
Sheila Schindler-Ivens<sup>6</sup> · Stacy Liebham<sup>4</sup> · John F. LaDisa Jr.<sup>1,7</sup>

Received: 15 January 2016 / Accepted: 21 June 2016  
© Springer-Verlag Berlin Heidelberg 2016

**Abstract** Image-based computational fluid dynamics (CFD) studies conducted at rest have shown that atherosclerotic plaque in the thoracic aorta (TA) correlates with adverse wall shear stress (WSS), but there is a paucity of such data under elevated flow conditions. We developed a pedaling exercise protocol to obtain phase contrast magnetic resonance imaging (PC-MRI) blood flow measurements in the TA and brachiocephalic arteries during three-tiered supine pedaling at 130, 150, and 170 % of resting heart rate (HR), and relate these measurements to non-invasive tissue oxygen saturation (StO<sub>2</sub>) acquired by near-infrared spectroscopy (NIRS) while conducting the same protocol. Local quantification of WSS indices by CFD revealed low time-averaged WSS on the outer curvature of the ascending aorta and the inner curvature of the descending aorta (dAo) that progressively increased with

exercise, but that remained low on the anterior surface of brachiocephalic arteries. High oscillatory WSS observed on the inner curvature of the aorta persisted during exercise as well. Results suggest locally continuous exposure to potentially deleterious indices of WSS despite benefits of exercise. Linear relationships between flow distributions and tissue oxygen extraction calculated from StO<sub>2</sub> were found between the left common carotid versus cerebral tissue ( $r^2 = 0.96$ ) and the dAo versus leg tissue ( $r^2 = 0.87$ ). A resulting six-step procedure is presented to use NIRS data as a surrogate for exercise PC-MRI when setting boundary conditions for future CFD studies of the TA under simulated exercise conditions. Relationships and ensemble-averaged PC-MRI inflow waveforms are provided in an online repository for this purpose.

✉ Laura Ellwein  
lellwein@vcu.edu

- <sup>1</sup> Department of Biomedical Engineering, Marquette University, 1515 West Wisconsin Ave, Milwaukee, WI 53233, USA
- <sup>2</sup> Department of Mathematics and Applied Mathematics, Virginia Commonwealth University, 1015 Floyd Ave, Richmond, VA 23284, USA
- <sup>3</sup> Department of Pediatrics, Herma Heart Center, Children's Hospital of Wisconsin, and the Medical College of Wisconsin, 9000 W Wisconsin Ave, Wauwatosa, WI 53266, USA
- <sup>4</sup> Department of Radiology, Children's Hospital of Wisconsin, 9000 W Wisconsin Ave, Wauwatosa, WI 53266, USA
- <sup>5</sup> Department of Exercise Science, Marquette University, 604 N. 16th St, Milwaukee, WI 53233, USA
- <sup>6</sup> Department of Physical Therapy, Marquette University, 604 N. 16th St, Milwaukee, WI 53233, USA
- <sup>7</sup> Division of Cardiovascular Medicine, Departments of Medicine and Physiology, Medical College of Wisconsin, 8701 Watertown Plank Road, Milwaukee, WI 53226, USA

## Abbreviations

|  |  |
|--|--|
| AAo  | Ascending aorta  |
| BF   | Blood flow   |
| BP   | Blood pressure   |
| BSA  | Body surface area  |
| CexO <sub>2</sub>                                      | Oxygen extraction  |
| CaO <sub>2</sub> , CtO <sub>2</sub> , CvO <sub>2</sub> | Arterial, tissue and venous oxygen concentration/content, respectively |
| CFD  | Computational fluid dynamics   |
| CHD  | Congenital heart disease   |
| CI   | Cardiac index  |
| CPET   | Cardiopulmonary exercise testing                                       |
| CO   | Cardiac output   |
| dAo  | Descending aorta   |
| FD   | Flow distribution  |
| HR   | Heart rate   |
| IA   | Innominate artery  |

|  |   |
|--|---|
| LCCA   | Left common carotid artery                                  |
| LSA  | Left subclavian artery                                      |
| MRI  | Magnetic resonance imaging                                  |
| NMF  | Normalized mean flow  |
| NIRS   | Near-infrared spectroscopy                                  |
| PC   | Phase contrast  |
| SaO <sub>2</sub> , StO <sub>2</sub> , SvO <sub>2</sub> | Arterial, tissue and venous oxygen saturation, respectively |
| TA   | Thoracic aorta  |
| TAWSS  | Time-averaged wall shear stress                             |
| WSS  | Wall shear stress   |

## 1 Introduction

Long-term cardiovascular morbidity is often present in patients with untreated congenital heart disease (CHD) and can persist even after repair, particularly for diseases of the thoracic aorta (TA) (Celermajer and Greaves 2002; Chatzis et al. 2008; Zanjani et al. 2008). The current paradigm for diagnosing the presence, severity, and success of a treatment for many congenital and acquired cardiovascular diseases often involves cardiac magnetic resonance imaging (MRI) while the patient rests within an MRI scanner. More recently, this imaging modality has also been coupled with computational fluid dynamics (CFD) modeling to quantify the potential for adverse hemodynamic forces including wall shear stress (WSS) (Kwon et al. 2014; Wendell et al. 2013). In one study of healthy young adults, areas of low time-averaged WSS (TAWSS) and elevated oscillatory shear index (OSI) were found in a rotating pattern progressing down the dAo (Frydrychowicz et al. 2009). A study of 10 middle-aged adults with preexisting plaques revealed similar WSS patterns that correlated with areas of atherosclerotic plaque (Wentzel et al. 2005). Indices of WSS continue to be linked to sites of atherosclerotic plaque formation in many arterial locations including the TA (LaDisa et al. 2011a,b; Samyn et al. 2015; Wentzel et al. 2005).

Unfortunately, MRI data acquired under resting conditions is not optimally representative of hemodynamics during normal daily activities such as ambulation or transient bouts of moderate exercise. Increased cardiac output (CO) and sympathetic nervous activity during exercise induce changes in tissue oxygen saturation (StO<sub>2</sub>), peripheral vascular resistance, arterial blood flow (BF), and WSS. Reduced exercise capacity is a comorbidity seen in specific populations of CHD that may manifest as hemodynamic abnormalities, underscoring the importance of CFD modeling under more physiologic (i.e. non-resting) conditions. Traditional cardiopulmonary exercise testing (CPET) is used to assess cardiorespiratory fitness and as an indicator of the severity and effectiveness of treatments for CHD, but it cannot provide detailed spatial and temporal quantification of hemo-

dynamic forces associated with cardiovascular disease. Thus, it is desirable to find a method to predict the severity of associated changes in local hemodynamics under exercise conditions, particularly for CHD patients.

Oxygen (O<sub>2</sub>) is a vasodilator in the systemic circulation, causing increased vessel diameter and decreased resistance (Boron and Boulpaep 2005; Hansen et al. 2000) with the net effect of increased BF in the setting of constant or increasing arterial-venous blood pressure (BP) gradient. Changes in tissue O<sub>2</sub> levels may trigger peripheral vascular changes during exercise (Ganong 2005; Gonzalez-Alonso et al. 2001). Correlations between BF, StO<sub>2</sub>, and vasodilation in vascular beds during exercise have been shown in various regions of the body under different types of exercise (Calbet et al. 2007; Gonzalez-Alonso et al. 2006, 2001). Near-infrared spectroscopy (NIRS) monitors StO<sub>2</sub> by using the differential absorption of near-infrared light to approximate the ratio of oxygenated to total hemoglobin in tissue. An initial purpose of NIRS was for determining cerebral StO<sub>2</sub> after injury or during surgery (Baris et al. 1995; Chakravarti et al. 2008), but its use has been extended to somatic regional StO<sub>2</sub> and perfusion assessment in a variety of clinical settings including the intensive care unit (Berens et al. 2006; Hoffman et al. 2004). A strong coupling between O<sub>2</sub> delivery and consumption during the transition from rest to exercise has been revealed by NIRS saturation data (Grassi et al. 2003; MacPhee et al. 2005). NIRS has also been recently incorporated into traditional CPET protocols to analyze regional oxygenation trends in children with and without CHD (Loomba et al. 2014; Rao et al. 2009, 2012). These findings suggest it may be possible to correlate somatic NIRS measurements of StO<sub>2</sub> during CPET with peripheral vascular changes during exercise for CFD-based prediction of upstream TA hemodynamics. This use requires an investigation with image-based CFD models created under various exercise levels, which is the central aim of the current work.

MRI during exercise has been pursued since the late 1990s. MRI has been used to quantify BF during supine cycle ergometry in the ascending aorta (AAo), pulmonary artery (Niezen et al. 1998; Weber et al. 2011), abdominal aorta (Pedersen et al. 1999; Steeden et al. 2010), and left ventricle (Sampath et al. 2011). Indices of WSS and CO were quantified in combination with CFD modeling in conjunction with a recumbent cycling protocol developed for imaging of the abdominal aorta (Cheng et al. 2003, 2004; Taylor et al. 2002). CFD was also used for patient-specific models of blood flow in the TA to quantify indices of WSS under simulated exercise conditions using changes in BF and resistance estimated from various literature sources (Kim et al. 2009b; LaDisa et al. 2011a). Unfortunately a standard protocol for imaging of the TA and its head and neck branches during exercise has not been established, resulting in a scarcity of data quantify-

ing preferential BF redistribution and peripheral resistance during increasing exercise levels.

Several recent investigations analyzed regulatory responses to cardiovascular events by complex modeling of arterial boundary conditions with a closed-loop circulation. These have been used to investigate autonomic responses to simulated abdominal aortic hemorrhage and cerebral aneurysm (Blanco et al. 2012), physiologic changes in the coronary and systemic arteries with light exercise (Kim et al. 2010), and baroreflex feedback during a tilt test (Lau and Figueroa 2015). While this approach adds complexity and likely a level of accuracy to the models themselves, these studies presented simulated results and involve single data sets. Moreover, these studies are typically based on, or rely on, ranges of physiologic values in applicable literature to assist in setting the parameters for these more complex boundary conditions, rather than utilize patient-specific data.

The objective of this prospective pilot study was twofold: (1) develop a protocol for obtaining phase contrast (PC) MRI velocity measurements in the TA and head and neck arteries during three-tiered supine submaximal cycling exercise; and (2) relate non-invasive measurements of StO<sub>2</sub> and oxygen extraction (CexO<sub>2</sub>) acquired during CPET using NIRS to peripheral vascular changes. These data will serve as the foundation for a procedure that could ultimately be used to set the inlet and outlet boundary conditions for subject-specific CFD modeling of the TA under non-resting conditions. The dissemination of this relationship for future use is also discussed.

## 2 Methods

Healthy young adult volunteers with no contraindications for MRI were recruited ( $n = 8$ ; 6 males, 2 females; mean age = 28, range = 24 – 35 years). Data sets from 2 male subjects were not analyzed due to anatomical variants of aortic arch branching pattern which made flow assessments in the brachiocephalic vasculature challenging. All procedures were approved by the Institutional Review Boards of Marquette University and Children's Hospital of Wisconsin, and written consent was obtained from all subjects.

### 2.1 Pedaling device

The pedaling device and setup used were modified from a prototype described in detail previously (Mehta et al. 2009). In brief, the pedaling device was a direct-drive, flywheel-equipped apparatus fabricated from non-metallic materials. Mechanical load was created by securing a nylon strap around the flywheel. The strap was adjustable to six different tension settings, thus creating six different frictional loads. Optical signals from an MR-compatible optical encoder (model

MR318, Micronor Inc., CA) corresponding to crank position were output via a fiber optic cable through a penetration panel to the controller unit (model MR 310, Micronor Inc., CA) located outside the scanner room. Position data were converted to electrical signals and sampled at 480 Hz using a laptop computer with a 12 bit analog to digital converter and data acquisition software (DI-158 and WINDAQ, respectively; DATAQ Instruments, Inc., Akron, OH).

For comparison with similar studies, the cyclic work associated with each frictional load was determined offline using specialized removable pedals equipped with force transducers and optical position encoders. Dynamic pedal position and normal and shear forces on each pedal were acquired under a constant pedaling rate at each load. Tangential forces were computed from normal and shear forces as well as pedal and crank position. Torque was computed as the product of the tangential forces and crank arm length. Cyclic work was calculated by integrating torque with respect to crank angle (Kautz and Brown 1998). All calculations were performed with custom MATLAB scripts (The Mathworks Inc., Natick, MA).

### 2.2 Experimental protocol

The experimental protocol (Fig. 1) consisted of a familiarization session followed by a pedaling protocol performed twice, first with the subject under NIRS testing, then again with the subject in the MR scanner. Currently available NIRS patches are not MRI compatible to enable safe scanning with these in place; hence, NIRS data were acquired from the same pedaling exercise protocol performed outside of the scanner.

#### 2.2.1 Familiarization session

After consent, subjects began with a familiarization session to set frictional load settings for generating target heart rates (HR) at each exercise level. Exercise target HRs for each subject were based on resting HR to best normalize results using the individual fitness levels of each subject, and to be achievable in the supine position (Denis and Perrey 2006; Poliner et al. 1980). Height and weight were recorded for calculation of body surface area (BSA) (Mosteller 1987). Resting supine HR was recorded once it had stabilized ( $\pm 10\%$ ) for  $\sim 1$  min. HR targets were set at 130, 150, and 170% of resting HR (henceforth referred to as HR<sub>130</sub>, HR<sub>150</sub>, HR<sub>170</sub>). The frictional load was then set for each subject at a low to moderate level such that a comfortable pedaling rate would cause the heart rate to increase and stabilize at HR<sub>130</sub>. Subjects were then instructed to pedal at levels of increasing load to achieve HR<sub>150</sub> and HR<sub>170</sub>. Frictional load settings were recorded for use in the subsequent MRI and NIRS cycling exercise protocol.

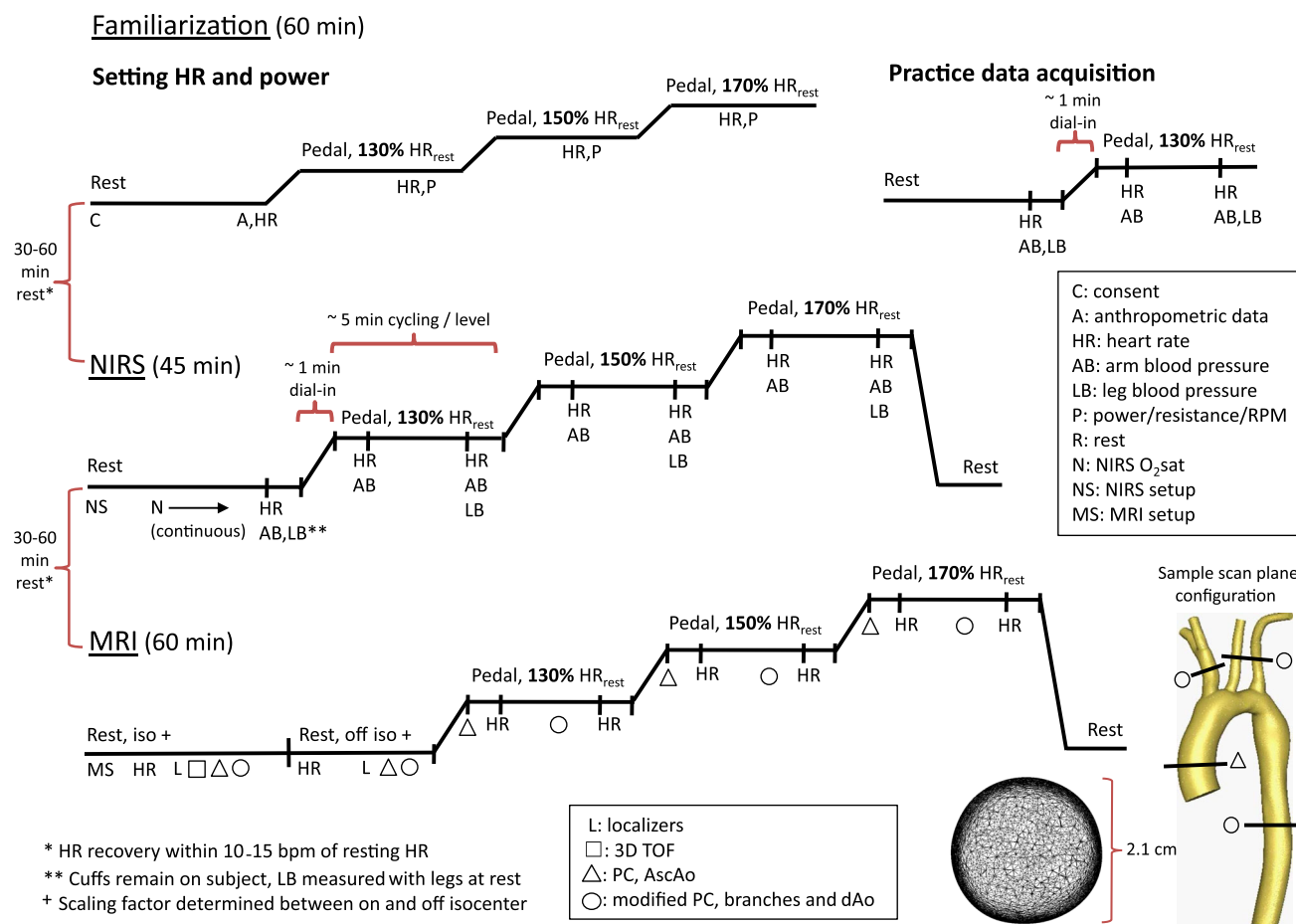


**Fig. 1** Experimental protocol. Please see the manuscript text for complete details. Briefly, a familiarization session was used to acclimate the subject and set target heart rate (HR) values through a balance of pedaling speed and resistance settings. Resting supine HR was recorded, and HR targets were set at 130, 150, and 170 % of resting HR (HR<sub>130</sub>, HR<sub>150</sub>, HR<sub>170</sub>). Subjects were then instructed to pedal at levels of increasing tension to achieve each of their three HR targets, during which the tension setting was recorded for use in the full protocol and for calculation of workload. The full protocol was performed once for NIRS and again during MRI after a 30–60 min rest period for HR to return to baseline. During the full protocol, subjects were asked to pedal such that HR<sub>130</sub> was reached ( $\pm 10\%$ ), at which point blood pressure or PC-MRI

sequences were performed. The PC-MRI imaging planes prescribed during rest were used at each HR target. Locations of these planes are shown in the CFD model on the lower right, together with a representative slice of the computational mesh from the descending aorta of one subject. This procedure was repeated for HR<sub>150</sub> and HR<sub>170</sub>. HR was recorded at the first and last minute of each exercise level for data analysis, and cycle position was recorded to calculate workload. C = consent; A = anthropometric data (height and weight), R = resistance; MS = MRI setup; L = localizers; open square 3D Navigator; open triangle PC-MRI of the AAo; open circle PC-MRI of the head and neck arteries

### 2.2.2 Pedaling exercise protocol

After familiarization and a rest period for HR recovery, subjects performed a custom supine pedaling protocol during which the subject's workload and HR increased for three 5-min exercise levels. After 3 min of resting baseline data collection, subjects were instructed to pedal such that HR<sub>130</sub> was reached, at which point either NIRS or PC-MRI data collection commenced. Subjects were verbally coached to alter their pedaling rate to maintain their target HR ( $\pm 10\%$ ) at load settings identified during the familiarization session. HR was recorded after one and 4 min of each level. Cycle position data were recorded as described previously. Power

(work/s) was calculated at each exercise level as the product of cyclic work determined offline and angular velocity (cycles/s) obtained from position data. At the end of HR<sub>130</sub>, the subject paused, while the load was increased according to the familiarization session, and the process was repeated for levels HR<sub>150</sub> and HR<sub>170</sub>. Motion of the torso was minimized for the duration of exercise.

### 2.2.3 NIRS setup and techniques

Subjects lay supine on an examination table with their head slightly elevated on a pillow. The subject's legs were extended toward the pedaling device at an angle amenable to ped-

aling similar to that in a prior NIRS protocol (Rao et al. 2009). Subjects were instrumented with a 12-lead electrocardiogram, automated oscillometric BP cuffs on the right arm and leg, and a pulse oximeter for arterial oxygen saturation (SaO<sub>2</sub>) on the right index finger (GE-Marquette, Waukesha, WI). One NIRS lead with 4 cm source-detector spacing and shallow-field rejection (INVOS 5100C, Somanetics Corporation, Troy, MI) was placed on each of the following locations: the midline forehead (cerebral), the left deltoid muscle (shoulder), just below the 12th rib (kidney), and on the left vastus lateralis muscle (leg) to measure regional StO<sub>2</sub>. NIRS data were acquired every 6 s. A snorkel-style mouthpiece was placed in the subject's mouth to monitor O<sub>2</sub> consumption and carbon dioxide production immediately before starting the *Pedaling Exercise Protocol*. Right arm BP was acquired after one and 4 min of each exercise level, and right leg BP was acquired immediately after each exercise level, while the legs briefly suspended pedaling and the load settings of the pedaling device were adjusted for the next exercise level.

#### 2.2.4 MRI setup and techniques

After a rest period for HR recovery, subjects were transferred to the Siemens 1.5 T MAGNETOM Symphony MRI scanner (Siemens USA, Malvern PA) with 6 channel anterior and posterior coils and initially positioned with the heart and TA at the magnet isocenter. The imaging protocol began with the subject at rest with 3 plane localizers allowing a respiratory navigated, 3D whole heart steady state free precession time-of-flight pulse sequence ("3D Navigator") for aortic morphology and phase contrast magnetic resonance velocity encoded imaging cine (PC-MRI) for blood flow assessment across the AAo, innominate artery (IA), left common carotid artery (LCCA), and left subclavian artery (LSA). Subjects were then repositioned off-isocenter so they could comfortably perform supine pedaling with sufficient clearance of their knees relative to the scanner bore. After re-localization with HASTE sequence, resting PC-MRI was repeated for each location (AAo, IA, LCA, LSA) in order to obtain a correction factor for off-isocenter flow assessments as discussed below. Subjects initiated the *Pedaling Exercise Protocol* after off-isocenter resting flow assessment. PC-MRI sequences were performed within each 5-min exercise interval at the same imaging planes prescribed during rest off-isocenter.

#### 2.2.5 Scan sequences

Imaging was performed using standard cardiac pulse sequences. Morphology was acquired with 3D Navigator with the following parameters: 9.6 ms repetition time, 1.9 ms echo time, 90° flip angle, 1.5 mm slice thickness, 24 × 32 cm<sup>2</sup> field of view, 1 excitation (1 NEX), and 256 × 173 matrix size. PC-

MRI was obtained at orthogonal scan planes in the AAo just above the aortic sinotubular junction and in the IA, LCCA, and LSA just above their origins from the aortic arch, as guided by the subject-specific 3D Navigator anatomic data. PC-MRI scan sequence parameters were selected for optimal image quality during sustained continuous exercise at multiple intensities. For all arteries these included: 28 ms repetition time, 3.3 ms echo time, 30° flip angle, 6 mm slice thickness, and 24 × 32 cm<sup>2</sup> field of view. Additional parameters for the AAo were: 3 NEX, 256 × 192 matrix size; and for the IA, LCCA, and LSA: 1 NEX, 256 × 125 matrix size.

### 2.3 CFD simulations

#### 2.3.1 Computational model construction

The 3D Navigator dataset from each subject was used to reconstruct geometrically representative computer models of the TA including the IA, LCCA, and LSA. 3D segmentation was favored over 2D segmentation for the non-contrast-enhanced imaging data obtained in this study and was performed using a semi-automated segmentation process within the open-source software ITK-SNAP ([www.itksnap.org](http://www.itksnap.org)) (Yushkevich et al. 2006). The region of interest outlining the TA was preprocessed and seeded with a series of 3D "snakes" (closed surfaces). The segmentation algorithm allowed snakes to propagate toward the artery wall according to user-defined parameters describing the evolution of forces (balloon, curvature, advection) that acted based on the shape of the snake and the image properties. Segmentation in the aorta was used to seed the segmentation in the head and neck branches. Preprocess and segmentation parameters were chosen to balance consistency between subject data sets and quality data reconstruction and are provided in the Appendix. The output of the segmentation process is a 3D VTK surface mesh (.vtk) of the lumen. Artery centerlines were extracted from the 3D surface meshes using native Python scripts in VMTK ([www.vmtk.org](http://www.vmtk.org)) (Antiga et al. 2008). Each 3D solid model of the TA and its branches was then queried using custom MATLAB scripts to create orthogonal segments defining the artery lumen. Artery segments and their centerlines were imported to Simvascular ([simtk.org](http://simtk.org)) and lofted to form the Parasolid model (Siemens, Plano, TX) characterizing the flow domain for the CFD mesh generation and modeling. The geometric model for each subject was the same for rest and each of the three exercise levels.

#### 2.3.2 Boundary conditions

Time-resolved volumetric BF was calculated from subject-specific PC-MRI data in the AAo using Segment (<http://segment.heiberg.se>) (Heiberg et al. 2010). Resulting AAo BF waveforms were imposed as model inlet boundary con-

ditions for resting and three exercising conditions using a time-varying plug velocity profile (Faggiano et al. 2013; Moireau et al. 2012). The ratio of mean flows at isocenter versus off-isocenter during rest was used to calculate a correction factor for each PC-MRI location to compensate for errors due to gradient inhomogeneities and concomitant gradients (Markl et al. 2003; Peeters et al. 2005) that may increase significantly with distance from the magnet isocenter.

The composite arterial behavior distal to the outlets of each model were modeled with a three-element Windkessel representation incorporating BP and BF measurements using the coupled-multidomain method and pulse pressure methods (Stergiopoulos et al. 1994, 1999; Vignon-Clementel et al. 2006), described in detail elsewhere (LaDisa et al. 2011a). Briefly, proximal characteristic resistance  $R_c$ , total arterial capacitance  $C$ , and distal resistance  $R_d$  were optimized for each outlet such that the BP waveform from each simulation corresponded with each subject's measured systolic, diastolic, and pulse BP under resting and three exercising conditions. Subject systolic and diastolic BP and resulting Windkessel parameters are presented in Table 1. An augmented-Lagrangian formulation (Kim et al. 2009a) for constraining the shape of the velocity profiles at model outlets was used to mitigate instabilities often occurring during flow deceleration and diastole. Vessel walls were modeled as rigid no-slip boundaries because of insufficient data to characterize the wall during exercise, including both changes in geometry and in material properties such as thickness and stiffness.

### 2.3.3 CFD simulations

Anisotropic meshes with unstructured tetrahedral elements were created for each model using an automatic adaptive mesh generation program (MeshSim, Simmetrix, Clifton Park, NY) capable of local adaptation (Muller et al. 2005; Sahni et al. 2006). Simulations were performed using the commercial flow solver LesLib (Altair Engineering Inc., Troy MI), which uses a stabilized finite element method to solve the conservation of mass and momentum balance equations. The Newtonian fluid assumption was applied with blood at constant viscosity (4 cP) and density (1.06 gm/cm<sup>3</sup>). Steady simulations under resting conditions using mean BF at rest for each subject were first performed on initial meshes with ~500k elements and maximum edge size of ~1 mm. Successive meshes were adaptively refined after each resting pulsatile simulation in order to distribute more elements near the surface of the lumen and in regions prone to greater flow disruption, reaching an intermediate mesh of ~3M elements after four adaptations. Results using each 3M element mesh and the highest exercising flow rate were used to adapt the mesh two more times to obtain a final mesh containing ~8M elements for each model, a size consistent with other current CFD models of the aorta (Dillon-Murphy et al. 2015).

This final mesh was used for simulations at rest and all three exercising flow rates for each subject. Convergence criteria included a minimum of 6 nonlinear iterations per time step with residuals  $\leq 10^{-3}$ . Simulations were conducted for 3–5 cardiac cycles until results were periodic with <1 mmHg difference in BP between equivalent time points in successive cycles.

## 2.4 Quantification

### 2.4.1 Blood flow

Mean BF were calculated from PC-MRI waveforms for each subject, exercise level, and vessel, then divided by BSA to normalize against body size (normalized mean flow, NMF). Cardiac output (L/min) and cardiac index (CI, L/min/m<sup>2</sup>) were equivalent to mean BF and NMF through the AAO, respectively. Mean BF in the descending aorta (dAo) was calculated as the AAO flow minus mean BF in the head and neck arteries, recognizing that the dAo flow includes internal mammary and intercostal flows not explicitly modeled here. The percent change in flow from resting values was computed to normalize against each subject's resting conditions and fitness level. The flow distribution (FD, % of cardiac output) and percent change in FD from rest were computed to quantify preferential redistribution of BF at each exercise level. Finally, total terminal resistance  $R$  at each outlet was calculated from mean BP and BF measurements as part of the determination of boundary conditions (see Sect. 2.3).

### 2.4.2 Hemodynamic indices

Time-averaged wall shear stress (TAWSS) and oscillatory shear index (OSI) were calculated (Les et al. 2010) and visualized using Paraview (Kitware, Inc., Clifton Park, NY) and MATLAB. Results were extracted at a nodal level both circumferentially and axially to obtain detail that may be more representative of the endothelium where changes in WSS manifest (Frydrychowicz et al. 2009; Malek et al. 1999). Locations for circumferential quantification included: 1 and 2 descending aorta outlet diameter (dAoD) lengths from the model inlet, 1 dAoD length after the LSA near the ligamentum arteriosum (LA1), 5 mm downstream (LA2), midway between the LSA and the outlet, 1dAoD length up from the outlet, and outlet edge (see Figs. 4 and 6). Circumferential WSS values were averaged in 16 equal-sized sectors across all subjects for each exercise level (LaDisa et al. 2011b). Locations for axial extraction occurred at 90 degree increments along the inner and outer curvatures of the aorta as well as the left and right luminal surfaces. Axial WSS values were smoothed using a moving average with window size equal to 1 dAoD. Values were then divided by the dAoD to normalize by subject (i.e. axial dimensions expressed as

**Table 1** Windkessel parameters for each subject

| Subject | Outlet | Rest |    |                |          |                | HR <sub>1.30</sub> |    |                |          |                | HR <sub>1.50</sub> |    |                |          |                | HR <sub>1.70</sub> |    |                |          |                |
|---------|--------|------|----|----------------|----------|----------------|--------------------|----|----------------|----------|----------------|--------------------|----|----------------|----------|----------------|--------------------|----|----------------|----------|----------------|
|         |        | SP   | DP | R <sub>c</sub> | C        | R <sub>d</sub> | SP                 | DP | R <sub>c</sub> | C        | R <sub>d</sub> | SP                 | DP | R <sub>c</sub> | C        | R <sub>d</sub> | SP                 | DP | R <sub>c</sub> | C        | R <sub>d</sub> |
| 1       | IA     | 120  | 60 | 406            | 1.76E-04 | 5231           | 127                | 69 | 225            | 1.43E-04 | 3790           | 146                | 68 | 394            | 8.48E-05 | 5240           | 156                | 64 | 38             | 4.48E-05 | 3811           |
|         | LCCA   |      |    | 1173           | 6.36E-05 | 14,461         |                    |    | 516            | 6.22E-05 | 8698           |                    |    | 855            | 3.92E-05 | 11,354         |                    |    | 108            | 1.60E-05 | 10,697         |
|         | LSA    |      |    | 723            | 1.03E-04 | 8912           |                    |    | 414            | 7.75E-05 | 6981           |                    |    | 641            | 5.22E-05 | 8516           |                    |    | 63             | 2.74E-05 | 6222           |
|         | dAo    |      |    | 75             | 8.57E-04 | 1085           |                    |    | 44             | 7.37E-04 | 734            |                    |    | 61             | 5.49E-04 | 810            |                    |    | 9              | 1.92E-04 | 890            |
|         | IA     | 96   | 48 | 506            | 1.50E-04 | 5112           | 103                | 60 | 299            | 7.95E-05 | 5037           | 113                | 61 | 340            | 3.36E-05 | 5726           | 115                | 58 | 321            | 5.09E-05 | 5406           |
| 2       | LCCA   |      |    | 1085           | 6.97E-05 | 10,971         |                    |    | 846            | 2.81E-05 | 14,257         |                    |    | 951            | 1.20E-05 | 16,032         |                    |    | 1035           | 1.58E-05 | 17,452         |
|         | LSA    |      |    | 718            | 1.05E-04 | 7255           |                    |    | 453            | 5.25E-05 | 7633           |                    |    | 514            | 2.22E-05 | 8666           |                    |    | 437            | 3.74E-05 | 7359           |
|         | dAo    |      |    | 144            | 5.25E-04 | 1456           |                    |    | 64             | 3.70E-04 | 1083           |                    |    | 49             | 2.32E-04 | 829            |                    |    | 47             | 3.46E-04 | 794            |
|         | IA     | 108  | 68 | 520            | 2.29E-04 | 6418           | 110                | 75 | 472            | 1.43E-04 | 7951           | 121                | 72 | 437            | 7.55E-05 | 7362           | 135                | 75 | 424            | 3.18E-05 | 7149           |
|         | LCCA   |      |    | 985            | 1.21E-04 | 12,145         |                    |    | 981            | 6.85E-05 | 16,543         |                    |    | 1271           | 2.60E-05 | 21,418         |                    |    | 1016           | 1.33E-05 | 17,131         |
| 3       | LSA    |      |    | 1077           | 1.11E-04 | 13,288         |                    |    | 1031           | 6.52E-05 | 17,385         |                    |    | 1398           | 2.36E-05 | 23,559         |                    |    | 829            | 1.63E-05 | 13,969         |
|         | dAo    |      |    | 132            | 8.40E-04 | 1758           |                    |    | 81             | 8.29E-04 | 1368           |                    |    | 71             | 4.65E-04 | 1196           |                    |    | 71             | 1.89E-04 | 1203           |
|         | IA     | 106  | 68 | 706            | 2.45E-04 | 8704           | 111                | 66 | 567            | 5.05E-05 | 9562           | 120                | 63 | 671            | 5.15E-05 | 8908           | 131                | 60 | 668            | 3.63E-05 | 6751           |
|         | LCCA   |      |    | 1278           | 1.35E-04 | 15,765         |                    |    | 955            | 3.00E-05 | 16,095         |                    |    | 976            | 3.54E-05 | 12,969         |                    |    | 1147.8         | 2.11E-05 | 11,607         |
|         | LSA    |      |    | 1353           | 1.28E-05 | 16,692         |                    |    | 682            | 4.20E-05 | 11,497         |                    |    | 706            | 4.89E-05 | 9382           |                    |    | 962            | 2.52E-05 | 9729           |
| 4       | dAo    |      |    | 174            | 9.93E-04 | 2143           |                    |    | 76             | 3.78E-04 | 1279           |                    |    | 90             | 3.84E-04 | 1193           |                    |    | 84             | 2.87E-04 | 851            |
|         | IA     | 88   | 40 | 468            | 1.22E-04 | 5767           | 99                 | 49 | 386            | 7.00E-06 | 6512           | 106                | 52 | 711            | 8.12E-06 | 6774           | 115                | 55 | 659            | 6.93E-06 | 6280           |
|         | LCCA   |      |    | 1073           | 5.30E-05 | 13,234         |                    |    | 60             | 4.10E-06 | 11,118         |                    |    | 1151           | 5.02E-06 | 10,963         |                    |    | 1586           | 2.88E-06 | 1511           |
|         | LSA    |      |    | 1433           | 3.94E-05 | 17,798         |                    |    | 917            | 2.95E-06 | 15,453         |                    |    | 1620           | 3.56E-06 | 15,429         |                    |    | 2603           | 1.76E-06 | 24,798         |
|         | dAo    |      |    | 122            | 4.66E-04 | 1507           |                    |    | 75             | 3.60E-05 | 1268           |                    |    | 117            | 4.93E-05 | 1115           |                    |    | 137            | 3.34E-05 | 1302           |
| 5       | IA     | 122  | 60 | 441            | 1.58E-04 | 5689           | 127                | 69 | 315            | 1.43E-04 | 4525           | 137                | 70 | 375            | 1.24E-04 | 4037           | 144                | 69 | 391            | 8.12E-05 | 4821           |
|         | LCCA   |      |    | 1054           | 6.90E-05 | 13,003         |                    |    | 807            | 5.59E-05 | 11,609         |                    |    | 1572           | 2.96E-05 | 16,919         |                    |    | 1620           | 1.96E-05 | 19,974         |
|         | LSA    |      |    | 703            | 1.04E-04 | 8668           |                    |    | 562            | 8.02E-05 | 8091           |                    |    | 1065           | 4.37E-05 | 11,461         |                    |    | 846            | 3.75E-05 | 10,434         |
|         | dAo    |      |    | 73             | 8.59E-04 | 1056           |                    |    | 85             | 5.31E-04 | 1223           |                    |    | 92             | 5.08E-04 | 987            |                    |    | 75             | 4.22E-04 | 928            |
|         | IA     | 122  | 60 | 441            | 1.58E-04 | 5689           | 127                | 69 | 315            | 1.43E-04 | 4525           | 137                | 70 | 375            | 1.24E-04 | 4037           | 144                | 69 | 391            | 8.12E-05 | 4821           |

Proximal characteristic resistance  $R_c$  (dynes/cm<sup>5</sup>), total arterial capacitance  $C$  (cm<sup>5</sup>/dynes), and distal resistance  $R_d$  (dynes/cm<sup>5</sup>) were optimized for each outlet such that the blood pressure waveform from each simulation corresponded with each subject's measured systolic and diastolic pressures (SP and DP, mmHg) under resting and three exercising conditions  
 IA innominate artery; LCCA left common carotid artery; LSA left subclavian artery; dAo descending aorta

**Table 2** Measurements of heart rate (HR) ( $R^2 = 0.99$ ), blood pressure (BP), cardiac output ( $R^2 = 0.99$ ), cardiac index ( $R^2 = 0.99$ ), and calculated workload for the collection of subjects studied

|                                       | Exercise level |                   |                      |                       |
|---------------------------------------|----------------|-------------------|----------------------|-----------------------|
|                                       | Rest           | HR <sub>130</sub> | HR <sub>150</sub>    | HR <sub>170</sub>     |
| HR (bpm)                              | 65 ± 2.5       | 86 ± 4.5*         | 97 ± 4.1*            | 111 ± 5.9*            |
| Systolic BP (mmHg)                    | 107 ± 5.4      | 113 ± 4.8         | 124 ± 6.1            | 131 ± 5.6*            |
| Mean BP (mmHg)                        | 78 ± 4.6       | 84 ± 4.5          | 90 ± 3.9             | 96 ± 5.0              |
| Diastolic BP (mmHg)                   | 57 ± 4.6       | 65 ± 3.7          | 64 ± 3.0             | 64 ± 3.1              |
| Cardiac Output (L/min)                | 6.2 ± 0.7      | 8.1 ± 1.1         | 8.9 ± 0.9            | 10.1 ± 1.1*           |
| Cardiac Index (L/min/m <sup>2</sup> ) | 3.1 ± 0.3      | 4.2 ± 0.4         | 4.7 ± 0.3*           | 5.2 ± 0.3*            |
| Workload (W)                          | Unloaded       | 15 ± 4*           | 25 ± 3* <sup>†</sup> | 38 ± 4* <sup>†§</sup> |

\*Significantly different from Rest; <sup>†</sup> significantly different from HR<sub>130</sub>; <sup>§</sup> significantly different from HR<sub>150</sub> (all  $p < 0.05$ )

$L/D$ ), and averaged across subjects for each exercise level. The location of the LSA was selected to be the zero location for  $L/D$ .

### 2.4.3 Oxygen saturation and extraction

NIRS time series were smoothed using a moving average with window size 5, corresponding to 30 s of data. Baseline resting  $StO_2$  was calculated as the mean of the 3 min of data prior to exercise. Mean  $StO_2$  for each exercise level was calculated as the average of the central 3 min of each 5-min interval. The INVOS NIRS oximeter assumes a three-to-one venous/arterial partitioning in cerebral and somatic tissues (Covidien 2009; Kurth and Uher 1997), thus venous saturation ( $SvO_2$ ) exiting each tissue bed was calculated as  $SvO_2 = (StO_2 - 0.25 \cdot SaO_2)/0.75$ . Partial pressure of oxygen (i.e.,  $PO_2$ ) was determined from a standard  $O_2$  dissociation curve (Boron and Boulpaep 2005; Varjavand 2000). An average value for the concentration of hemoglobin  $Hb = 14.8$  g/dL was used for all subjects and assumed to be constant over the course of the protocol (Voight et al. 2007). Oxygen content ( $cO_2$ , ml/dl) of arterial and venous locations was calculated based on  $SO_2$ ,  $CtO_2 = (1.34 \times Hb \times SO_2 \times 0.01) + (0.003 \times PO_2)$  (Boron and Boulpaep 2005). Oxygen contents  $CaO_2$ ,  $CtO_2$ , and  $CvO_2$ , arterial-venous difference ( $CavO_2 = CaO_2 - CvO_2$ ), and  $O_2$  extraction ( $CexO_2 = CavO_2/CaO_2$ ) were calculated. Finally, % change in  $CexO_2$  from rest was calculated for correlation with flow indices at each exercise level.

### 2.5 Statistical and regression analysis

Statistical analysis across the pool of six subjects was conducted on the quantified indices detailed above. Values were expressed as mean ± standard error. Comparison of means between exercise levels including rest was conducted with one-way ANOVA using Tukey–Kramer post-hoc analysis, with  $p < 0.05$  considered statistically significant.

Each branch vessel outlet was associated with a NIRS probe site based on downstream tissue vascular beds: the LCCA with cerebral tissue, the LSA with shoulder tissue, and the dAo with leg tissue. Regression was used to determine relationships between flow indices and  $CexO_2$  for each branch-tissue pair. These relationships are disseminated with ensemble-averaged AAO PC-MRI waveforms at rest and each exercise level via an online repository ([www.datadryad.org](http://www.datadryad.org)).

## 3 Results

### 3.1 Aggregate measurements

All subjects successfully achieved their three target HRs. Average resting HR for the six subjects was  $65 \pm 2.5$  bpm, with linear increases ( $R^2 = 0.99$ ) to  $86 \pm 4.5$ ,  $97 \pm 4.1$ , and  $111 \pm 5.9$  bpm during successive increases in exercise intensity. CO and CI increased with respect to HR level ( $R^2 = 0.99$ ) from  $6.2 \pm 0.7$  L/min to  $8.1 \pm 1.1$ ,  $8.9 \pm 0.9$ , and  $10.1 \pm 1.1$  L/min, and from  $3.1 \pm 0.3$  to  $4.2 \pm 0.4$ ,  $4.7 \pm 0.3$ , and  $5.2 \pm 0.3$  L/min/m<sup>2</sup> respectively. SBP and MBP increased as expected with exercise level, and DBP leveled off after the first exercise level HR<sub>130</sub>. Average workloads were  $15 \pm 4$ ,  $25 \pm 3$ , and  $38 \pm 4$  W at successive exercise levels. Significant values are indicated in Table 2.

### 3.2 Hemodynamics

Inflow waveforms in the AAO quantified from PC-MRI for each subject at rest and HR<sub>130</sub>, HR<sub>150</sub>, HR<sub>170</sub> are shown in Fig. 2. In general, the length of diastole and thus the length of the cardiac cycle decreased as HR increased, with reduced retrograde (backwards) diastolic flow and increased peak systolic flow. The 3D solid model reconstruction of each subject's TA, IA, LCCA, and LSA are shown next to each set of waveforms. Branch vessels were terminated at locations of declining image quality.

NMF and FD at each of the three HR levels expressed as percent of resting values are depicted in Fig. 3a, b. In

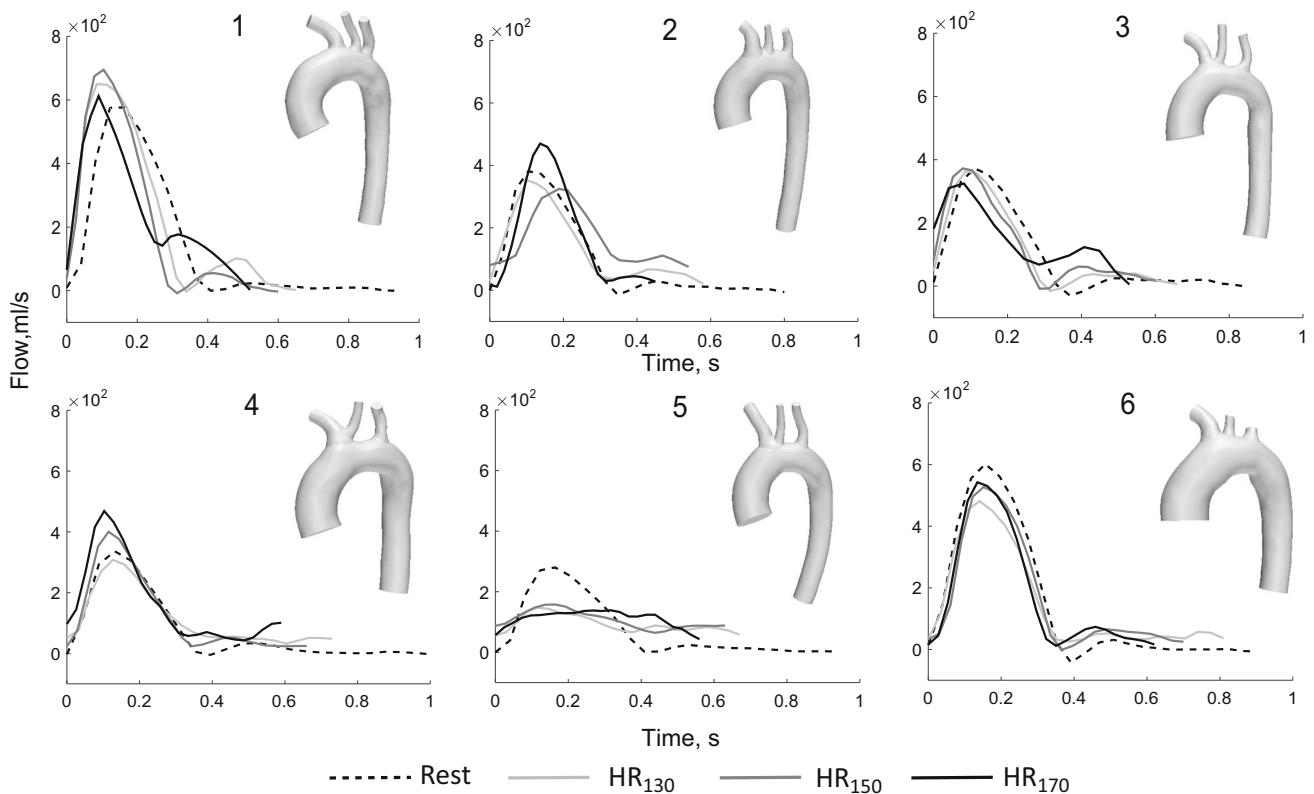


**Fig. 2** Inflow waveforms in the ascending aorta as quantified from PC-MRI for each subject at rest and at 130, 150, and 170 % of resting heart rate (HR<sub>130</sub>, HR<sub>150</sub>, HR<sub>170</sub>). In general, the length of diastole and the cardiac cycle decreased as HR increased, with reduced retrograde flow and increased flow at peak systole. The waveforms for each patient

are accompanied by the 3D solid model created from MRI data of the subject's thoracic aorta and head and neck arteries. Ensemble-averaged versions of inflow waveforms at rest, HR<sub>130</sub>, HR<sub>150</sub>, and HR<sub>170</sub> have been created from this data and disseminated through an online repository for use in related CFD studies (see text)

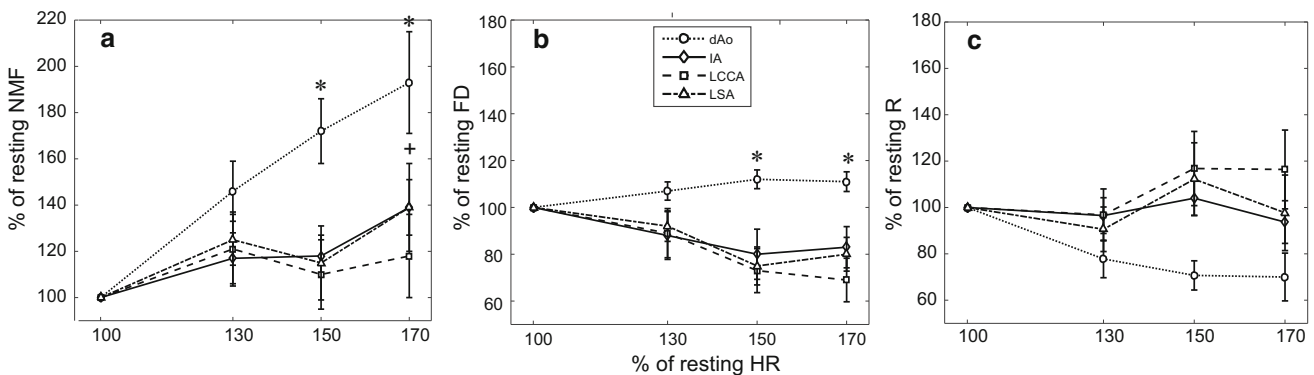


**Fig. 3** **a** Normalized mean flow (NMF), **b** flow distribution (FD), and **c** vascular resistance (*R*) expressed as percent of resting values at each of the three heart rate (HR) levels in the innominate (IA), left common

carotid (LCCA), and left subclavian (LSA) arteries and descending aorta (dAo). \*Significantly different from Rest, dAo; + significantly different from Rest, IA (all  $p < 0.05$ )

the dAo, NMF increased linearly with respect to HR ( $R^2 = 0.99$ ) by 46, 72, and 93 %, with significance at HR<sub>150</sub> and HR<sub>170</sub>. The IA showed increases in NMF of 17, 18, and 39 %, with significance only at HR<sub>170</sub>. Increases in NMF in the LCCA and LSA were 21, 10, and 18 %, and 25, 15, and 39 %, respectively, but were not statistically significant. FD

to the dAo increased by 7, 12, and 11 % with respect to FD at rest, with significance at HR<sub>150</sub> and HR<sub>170</sub>. Increases in FD to the dAo were accompanied by decreases to the head and neck arteries. FD decreased in the IA, LCCA, and LSA by 12, 20, and 17 %; 11, 27, and 31 %; and 8, 25, and 20 %; but without significance in all cases. The percent of resting

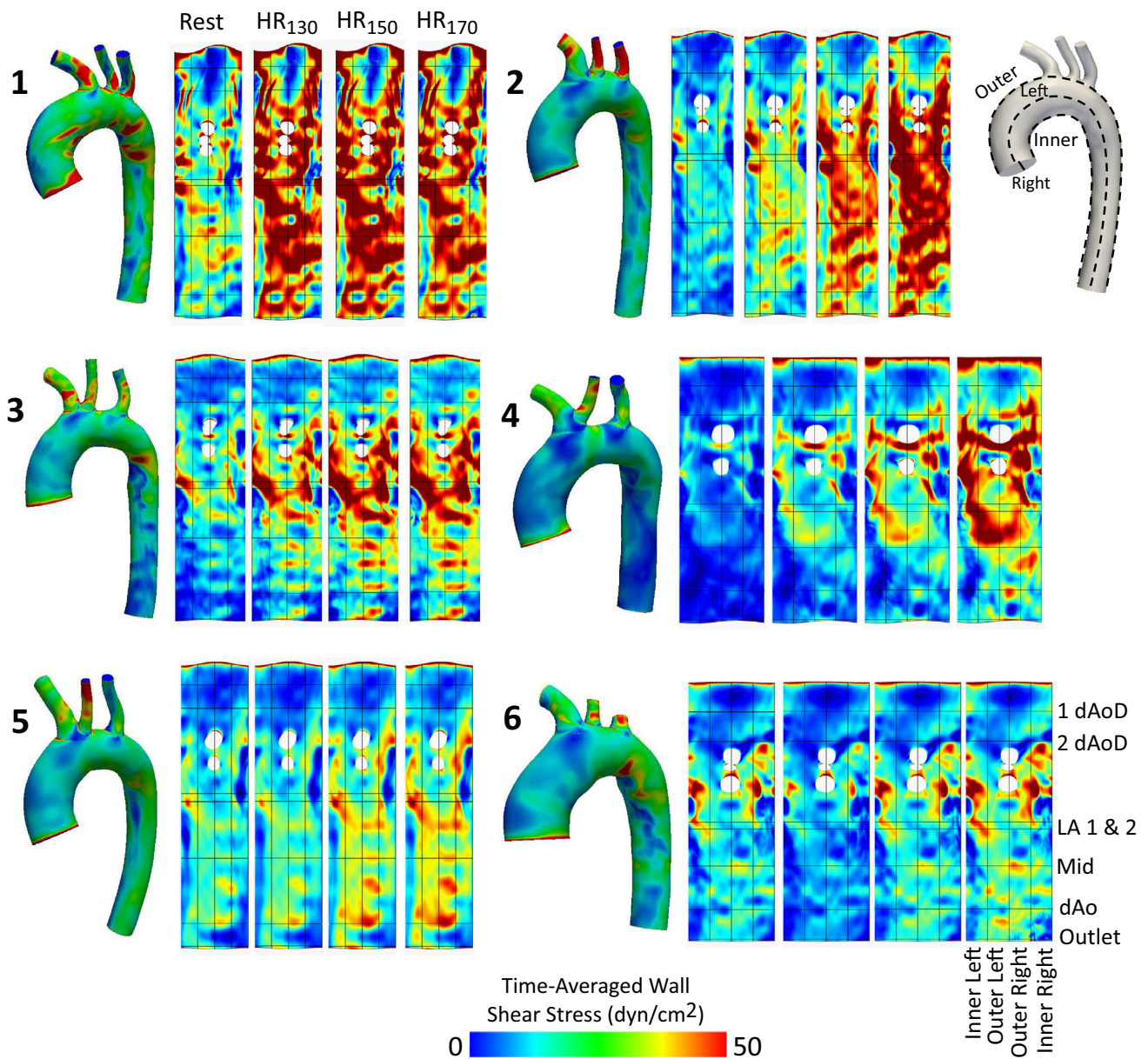


**Fig. 4** Distributions of TAWSS for the healthy adult subjects in this investigation (labeled 1–6). Resting distribution is shown on the 3D model of each patient. For clarity, unwrapped TAWSS distributions are also provided for the complete thoracic aorta at rest and each of the three exercise levels

vascular resistance decreased in the dAo at each exercise level as seen in Fig. 3c. In the head and neck arteries, resistance decreases slightly at HR<sub>130</sub>, increases dramatically at HR<sub>150</sub>, then recovers to resting levels in the LSA and IA but remains elevated in the LCCA.

### 3.3 CFD simulations

Spatial distributions of TAWSS are shown in Fig. 4. In general, regions of higher TAWSS are seen in the narrower brachiocephalic arteries, through the aortic arch, and on the

**Table 3** Mean flows in units of L/min for each subject as calculated from PC-MRI measurements

| Subject | Mean flow (L/min) |                   |                   |                   |
|---------|-------------------|-------------------|-------------------|-------------------|
|         | Rest              | HR <sub>130</sub> | HR <sub>150</sub> | HR <sub>170</sub> |
| 1       | 8.1               | 13.4              | 12.5              | 14.5              |
| 2       | 5.6               | 7.9               | 9.8               | 10.3              |
| 3       | 5.4               | 6.6               | 7.5               | 8.7               |
| 4       | 4.2               | 6.7               | 7.4               | 10.0              |
| 5       | 5.2               | 5.6               | 6.4               | 6.4               |
| 6       | 8.4               | 8.7               | 10.0              | 10.7              |

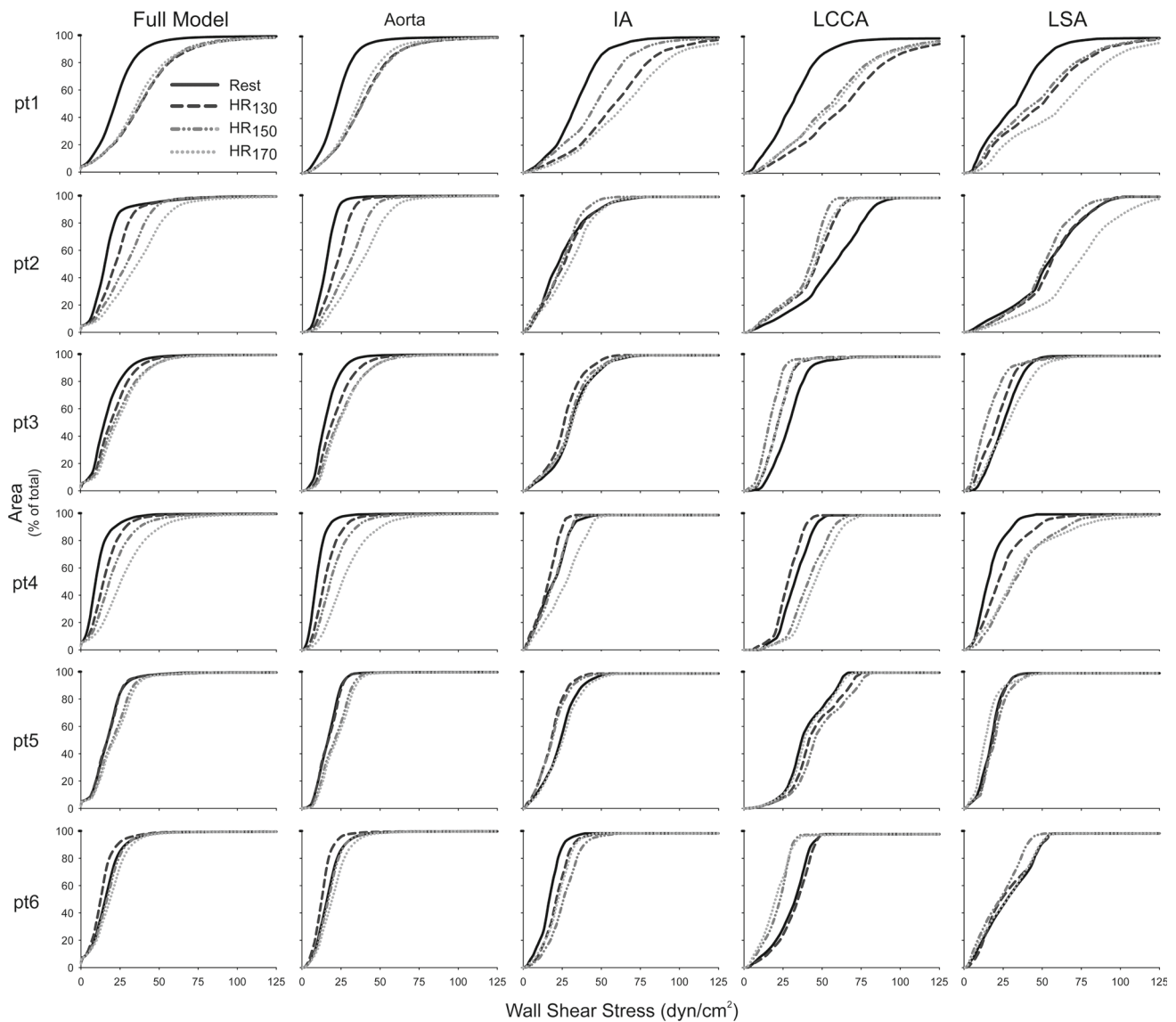


**Fig. 5** Cumulative percentage distributions of the total area exposed to values of TAWSS from 0–125 dyn/cm<sup>2</sup> at rest as well as 130, 150, and 170 % of resting heart rate (HR<sub>130</sub>, HR<sub>150</sub>, HR<sub>170</sub>) for CFD simulations of the healthy adult subjects in this investigation (labeled 1–6). Each location on a curve represents the percentage of the vessel's total area

exposed to TAWSS below that particular TAWSS value. Differences in the total area at TAWSS values from approximately 5–75 dyn/cm<sup>2</sup> occur with exercise. The redistribution of TAWSS values within this range depended on the patient, but primarily occur in the TA as a result of increases in flow to the dAo during exercise

outer curvature of the dAo, while lower TAWSS is found on the outer curvature of the AAo and on the inner curvature of the dAo. The differences between exercise levels are also depicted from the 2D unwrapped panels shown in Fig. 4. Increases in mean flow (Table 3) were generally associated with increased TAWSS, but did not significantly change the 2D pattern of TAWSS.

Figure 5 shows the cumulative percentage distribution of the total area exposed to values of TAWSS from 0–125 dyn/cm<sup>2</sup> (bin size of 0.5 dyn/cm<sup>2</sup>) at rest as well as HR<sub>130</sub>, HR<sub>150</sub>, and HR<sub>170</sub>. Each location on the curve represents the percentage of the vessel's total area exposed to TAWSS

below that particular TAWSS value. These plots are a manifestation of the collective HR, CO, FD and TAWSS results presented above. Differences in the total area at TAWSS values from approximately 5–75 dyn/cm<sup>2</sup> occur with exercise. Comparison of the cumulative percentage distributions from the full model of each subject to the respective arteries within each model reveals that the redistribution of TAWSS values within this range depends on the subject, but primarily occurs in the TA as a result of increases in FD to the dAo with each exercise level.

Patterns of OSI also remained similar between exercise levels (Fig. 6) for a given subject, but with more localized

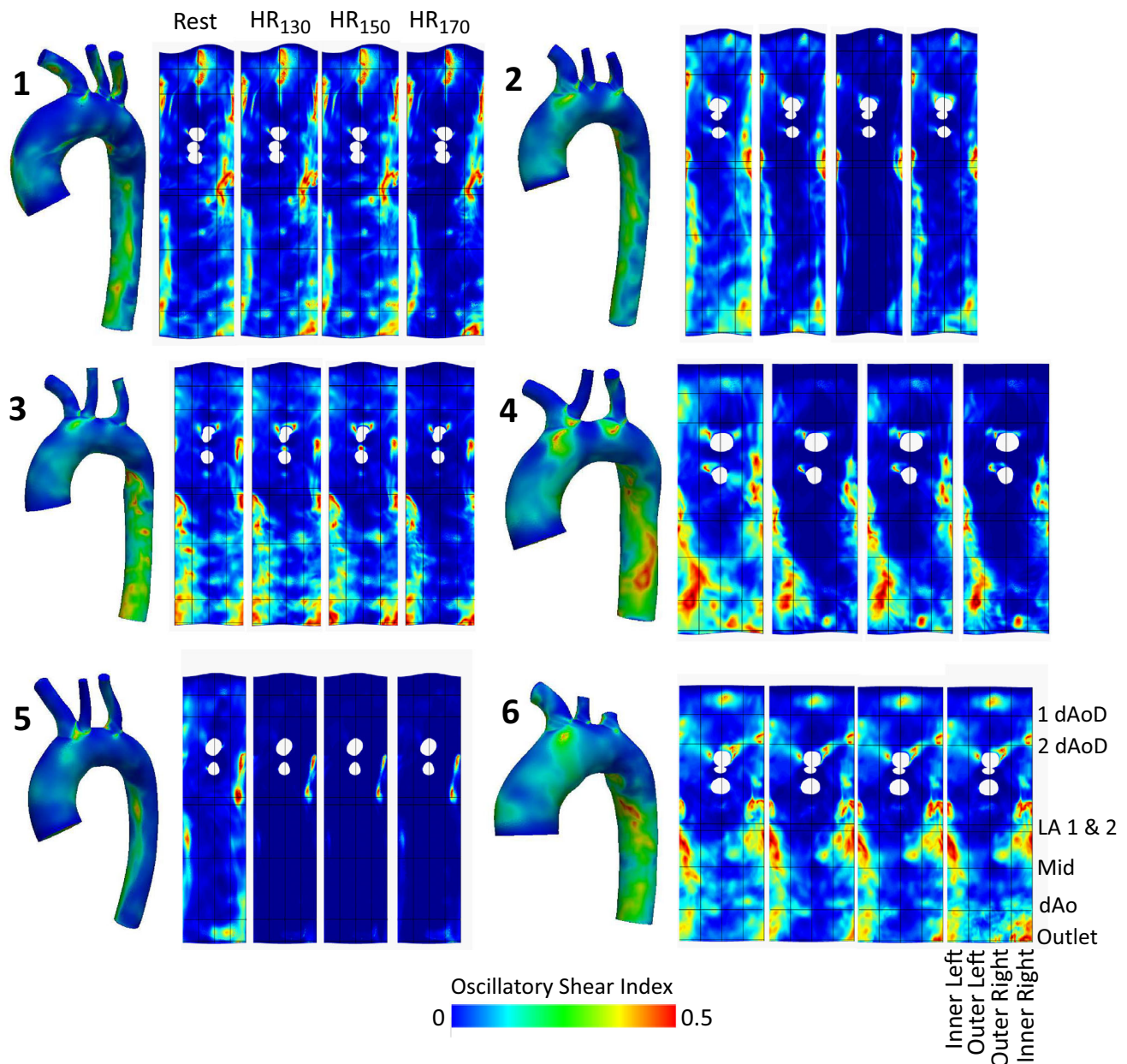


**Fig. 6** Distributions of OSI for the healthy adult subjects in this investigation (*labeled 1–6*). Resting distribution are shown on the 3D model of each patient. For clarity, unwrapped OSI distributions are also provided for the complete thoracic aorta at rest and each of the three exercise levels

variability compared to TAWSS. Unwrapped OSI results generally showed a decrease in OSI with increases in mean BF with several exceptions. For example, subject 2 had the lowest OSI but the second-highest BF occurring at HR<sub>150</sub>. Similarly, OSI remained low for all three exercise levels for subject 5, whereas mean BF increased appreciably between rest, HR<sub>130</sub>, and HR<sub>150</sub>. In these instances, the subjects did not experience retrograde flow during the times when the flows were measured.

### 3.4 Local quantification

Figure 7 (right) shows local quantification of TAWSS in the TA for the inner, left, outer, and right curvatures of the aorta as well as the head and neck arteries (middle). As anticipated, the lowest TAWSS values generally occur under resting conditions and increase with exercise level. When viewing results axially (i.e., longitudinally), elevated TAWSS was observed on the outer curvature between 0 and 2 diam-

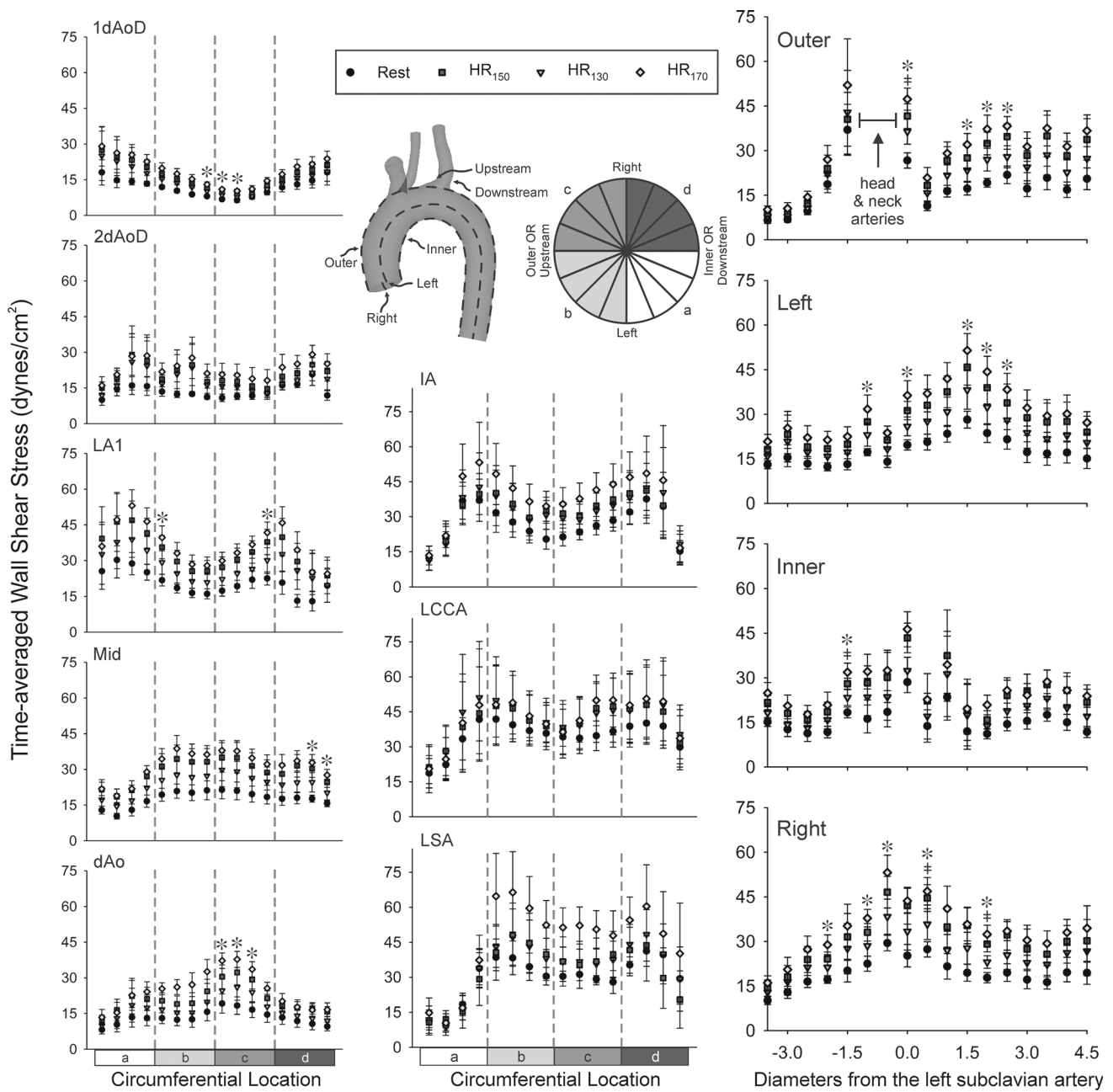


**Fig. 7** Circumferential TAWSS results for locations in the thoracic aorta (left column) were extracted and plotted at 1 and 2 descending aorta outlet diameter (dAoD) lengths up from the ascending aorta inlet, 1 dAoD length after the LSA in the region of the ligamentum arteriosum (LA1) midway between the LSA and the outlet, 1 dAoD upstream from the outlet, and the outlet edge. Circumferential results were averaged in 16 equal-sized sectors. Circumferential results were similarly obtained for each head and neck artery one diameter from their bifurcation off the aorta (middle column). Axial TAWSS results throughout the aorta (right

column) were extracted and plotted along the outer and inner curvatures of the thoracic aorta, as well as the anatomic left and right surfaces. The plots shown are ensemble-averaged from spatially equivalent locations of each patient at rest and three exercise levels. Results were smoothed using a moving average with window size equal to 1 dAoD for each subject's aorta. Values were then divided by the dAoD to normalize by subject (i.e., expressed as  $L/D$ ). The location of the LSA was selected to be the zero location for  $L/D$ . \*HR<sub>150</sub> significantly different from Rest; †HR<sub>170</sub> significantly different from Rest (all  $p < 0.05$ )

eters proximal to the LSA, where flow abruptly entered the more narrow head and neck branches. The outer and right curvatures also show higher TAWSS distal to the branches vs proximal. Figure 7(left) also shows ensemble-averaged cir-

cumferential quantification of TAWSS in the aorta for each of 6 cross-sectional locations. Again the lowest TAWSS values occur under resting conditions then progressively increase with exercise. In some cases, moderate peaks in TAWSS

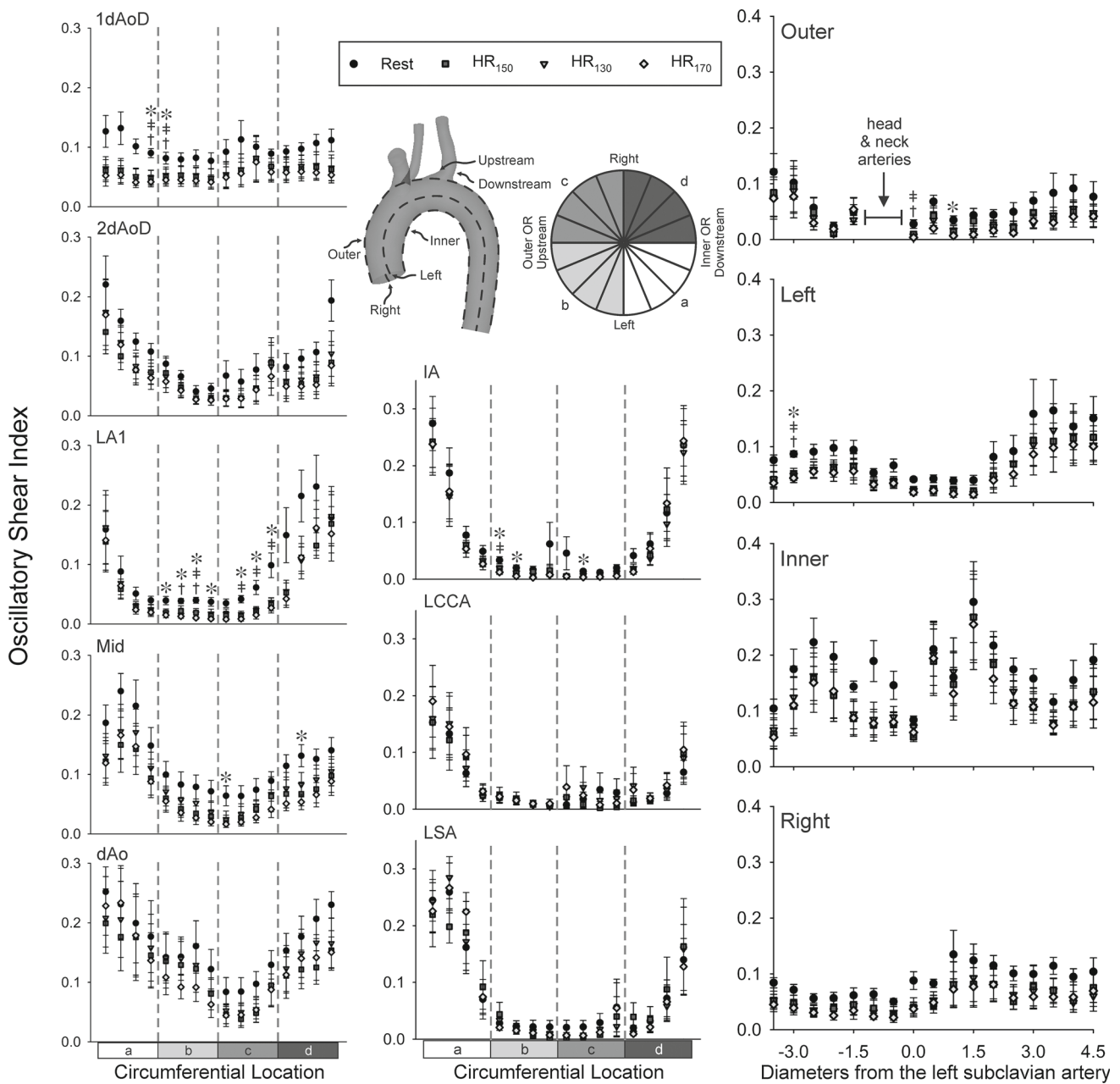


**Fig. 8** Circumferential results for locations in the thoracic aorta (*left column*) were extracted and plotted at 1 and 2 descending aorta outlet diameter (dAoD) lengths up from the ascending aorta inlet, 1 dAoD length after the LSA in the region of the ligamentum arteriosum (LA1), midway between the LSA and the outlet, 1 dAoD upstream from the outlet, and the outlet edge. Circumferential results were averaged in 16 equal-sized sectors. Circumferential results were similarly obtained for each head and neck artery one diameter from their bifurcation off the aorta (*middle column*). Axial OSI results throughout the aorta (*right column*) were extracted and plotted along the outer and inner curvatures

of the thoracic aorta, as well as the anatomic left and right surfaces. The plots shown are ensemble-averaged from spatially equivalent locations of each patient at rest and three exercise levels. Results were smoothed using a moving average with window size equal to 1 dAoD for each subject's aorta. Values were then divided by 1 dAoD to normalize by subject (i.e., expressed as  $L/D$ ). The location of the LSA was selected to be the zero location for  $L/D$ . †HR<sub>130</sub> significantly different from Rest; ‡HR<sub>150</sub> significantly different from Rest; \*HR<sub>170</sub> significantly different from Rest (all  $p < 0.05$ )

at rest are more pronounced at all levels of exercise (e.g.; 2dAoD inner left and outer left regions, LA1 and LA2 inner left and right regions). Ensemble-averaged circumferential results in the head and neck vessels (Fig. 7, middle) indicate

no increase in TAWSS on the anterior surface at any exercise level for all branches, with TAWSS remaining at 10–20 dyn/cm<sup>2</sup>. TAWSS at HR<sub>130</sub> and HR<sub>150</sub> are similar on the posterior surface in the IA and LSA, but at rest and at HR<sub>170</sub>

are appreciably lower and higher, respectively. It should be noted that in subjects 4 and 5, the LCCA branches off in close proximity to the IA as in a bovine arch, which may influence results.

Figure 8 shows ensemble-averaged local quantification of OSI in the aorta for the inner, left, outer, and right curvatures of the aorta. Axial OSI values in the aorta between exercise levels are similar but distinct from values at rest. The highest values for OSI are observed on the inner curvature (top right panel) and are nearly identical 0 and 2 diameters distal to the LSA even with the influence of exercise. This behavior is also evident from the circumferential results at LA1, with the high OSI at the inner curvature (farthest left and right data points) remaining above 0.15 and not decreasing much with exercise. Of particular interest is evidence of a helical pattern of OSI from local circumferential quantification. Comparing OSI at the ligamentum arteriosum (LA1) vs. distal locations (mid, dAo), the peak OSI of ~0.25 shifts from the inner right to the inner left of the aorta at midway then to the inner curvature at dAo close to the outlet. With the exception of the posterior surface of the IA, likely from influence of the LCCA branching off the IA in two subjects, circumferential OSI results are not significantly different between exercise levels for all three arch branches.

### 3.5 Oxygen extraction and NIRS-derived surrogates (NDS)

Figure 9a shows the change in CexO<sub>2</sub> from rest for all four regions. Brain and kidney CexO<sub>2</sub> both decreased linearly with exercise level ( $R^2 = 0.99$  and  $0.98$ , respectively) and with significance vs. rest at HR<sub>150</sub> and HR<sub>170</sub>. Leg CexO<sub>2</sub> increased the most from rest to HR<sub>130</sub> then appeared to stabilize. Shoulder CexO<sub>2</sub> was relatively constant for the first exercise level. Although shoulder CexO<sub>2</sub> increased at higher levels, these changes did not reach significance.

NIRS-derived surrogates were determined for eventual use in CFD modeling by relating the % change in FD at a given vessel outlet ( $y$ ) to the % change in CexO<sub>2</sub> in a corresponding tissue bed ( $x$ ). Linear regression determined the following relationships (Fig. 9b):

$$\text{LCCA and brain: } y = 1.61x - 0.61, \quad R^2 = 0.96$$

$$\text{dAo and leg: } y = 0.53x + 0.47, \quad R^2 = 0.87$$

No correlation was observed between the shoulder CexO<sub>2</sub> and LSA flow (Fig. 9d) despite the LSA being the primary artery feeding the shoulder vasculature. These relationships are disseminated with ensemble-averaged AAO PC-MRI waveforms and Windkessel parameters at rest and each exercise level via an online repository ([www.datadryad.org](http://www.datadryad.org)).

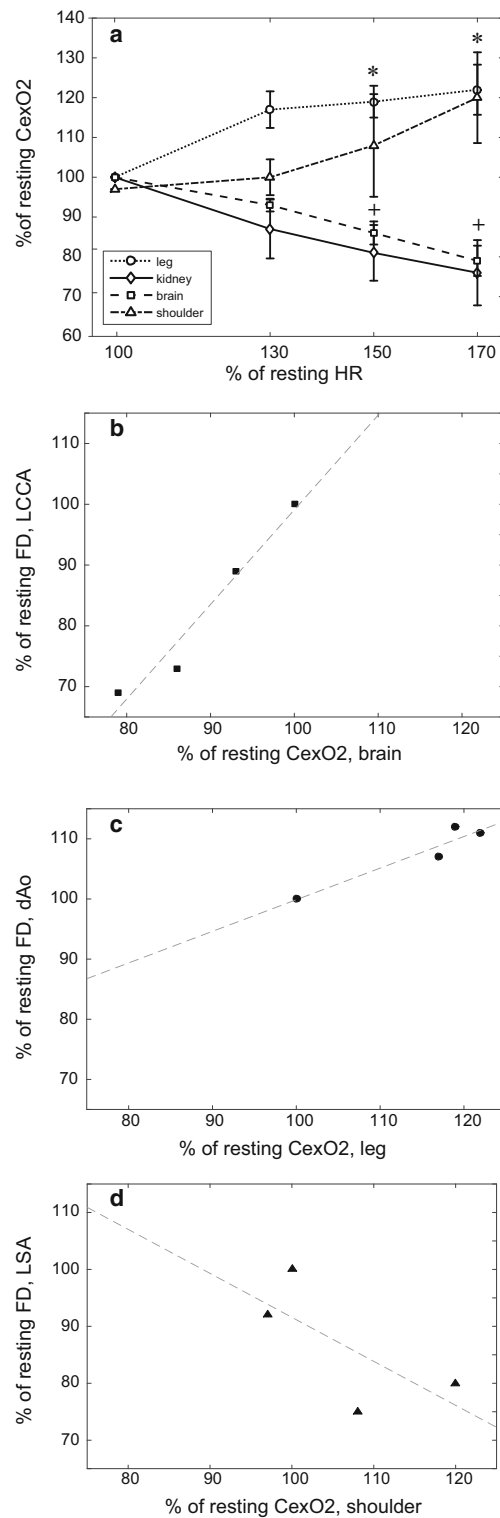


**Fig. 9** a Oxygen extraction expressed as percent of resting values at each of the three heart rate (HR). \*Significantly different from Rest, leg; + significantly different from Rest, brain (all  $p < 0.05$ ). b–d Correlations between percent change in mean blood flow in the left common carotid (LCCA, b) the descending aorta (dAo, c) and the left subclavian (LSA, d) arteries versus percent change in CexO<sub>2</sub> in the tissues (brain, leg, and shoulder, respectively)

## 4 Discussion

Indices of WSS in the TA can be quantified at rest using MR imaging, and low WSS has been seen with sites of plaque formation. However, alterations in hemodynamics under more realistic conditions such as ambulation or aerobic exercise are more difficult to discern by imaging. A custom three-tiered supine pedaling protocol was thus designed to quantify preferential blood flow re-distribution and alterations in hemodynamics in the AAo, IA, LCCA, LSA, and dAo using PC-MRI and CFD modeling and relate to regional tissue oxygenation acquired with NIRS during rest and exercise. Advantages of this approach include the use of subject-specific MRI data for 3D model and boundary condition generation with particular application to CFD, acquired at multiple levels of real-time exercise and for a group of subjects. The resulting data are then used here in boundary conditions that provide CFD results for the current work, rather than just presented for potential use in CFD modeling at a later time. Connecting PC-MRI data with regional tissue oxygenation acquired with near-infrared spectroscopy supports the eventual goal of using NIRS data as a surrogate for exercise MRI in subject-specific CFD modeling and in the clinic. This investigation marks the first known quantification of changes in CO and the preferential re-distribution of blood flow in the TA and head and neck arteries by PC-MRI during supine exercise of increasing intensity.

### 4.1 Exercise hemodynamics

Exercise activates the sympathetic nervous system, increasing HR and cardiac contractility while inducing global peripheral vasoconstriction (Boron and Boulpaep 2005). These actions increase cardiac output and direct blood flow and oxygen to exercising skeletal muscle while restricting blood flow to non-exercising regions such as the renal and gastrointestinal systems. Macdonald et al. (2015) recently presented results using an MR-compatible stepping device on a group of 12 healthy adult volunteers in which systolic peak flow increased by 15% with exercise at 43W, similar to our findings of ~10%. Niezen et al. (1998) and Cheng et al. (2004) showed that the amount of retrograde diastolic flow and the time in diastole decreased with increased heart rate and mean flow, consistent with sympathetic activation during exercise (Westerhof et al. 2005). Niezen et al also reported a 57% increase in cardiac output from rest to 50 W, and Weber et al found a 61% increase from rest to 180% HR increase (Weber et al. 2011), both of which are consistent with the increase in cardiac output found in the current investigation.

Results of the current investigation indicate that the metabolic needs of active leg muscles during cycling exercise were met with requisite increased BF and decreased

resistance in the dAo that impact the total area of potentially adverse TAWSS. Flow to the LCCA during exercise also generally increased above resting values, consistent with previous observations during submaximal exercise (Thomas et al. 1989). Flow to the LSA and IA increased as well, in contrast to the decrease in brachial artery flow observed by Green et al during seated cycling (Green et al. 2002), but in line with brachial flow reported by Tanaka et al. (2006) and subclavian vein flow (Calbet et al. 2007). Flow distribution to the head and neck arteries toward non-exercising vascular beds generally decreased and resistance in these arteries increased as expected. Slight increases in flow distribution and decreases in resistance to the IA and LSA observed at the highest exercise level may be related to intermittent tensing of arm muscles during cycling increasing metabolic demand. Interestingly, resistance in the LCCA increased dramatically at HR<sub>150</sub> and remained elevated. Enhanced blood flow to cerebral vascular beds in excess of oxygen demand (Querido and Sheel 2007) may be mitigated by vasoconstriction at higher exercise levels.

### 4.2 Wall shear stress metrics

PC-MRI has been used with CFD studies in recent years to quantify changes in arterial hemodynamics during rest and simulated exercise conditions, yet this is the first CFD analysis of the TA and head and neck arteries using measured subject-specific data during exercise. In prior studies, CFD models from adults undergoing simulated exercise at 150% of resting HR showed significant localized increased WSS and decreased OSI in the abdominal aorta (Tang et al. 2006). Similar results have been seen in the TA with simulated exercise (LaDisa et al. 2011a). While TA hemodynamics have also been quantified using MRI and CFD for patients with aortic coarctation at rest (Frydrychowicz et al. 2008; Ladisa et al. 2010), the current results for measured changes using these combined tools during multiple levels of exercise are the first of their kind to be published.

The detailed 3D and unwrapped 2D results displayed here at three different exercise levels uncover instances of TAWSS increasing with mean BF (Table 3; Fig. 4). CFD results also revealed favorable reductions in OSI corresponding to more unidirectional inflow with exercise at any level (Figs. 2, 7). This finding may suggest that the benefits of exercise include increased unidirectional flow, which minimizes OSI or variations in TAWSS. These favorable hemodynamic changes in the TA and its branches may occur at low exercise levels, as suggested by current research, and may not require more rigorous exercise to become manifest. As shown by others, helical flow has a positive physiologic role by facilitating blood flow transport and minimizing residence time for atherogenic substances like lipoprotein particles, monocytes and platelets (Liu et al. 2015).

Results from axial and circumferential quantification averaged across the subject population confirm prior studies performed with control subjects compared against treated coarctation patients (LaDisa et al. 2011b) and with simulated exercise (LaDisa et al. 2011a), and uncover more detailed information of potential importance. Increasing levels of submaximal exercise generally correspond with appreciably increased TAWSS in the aorta except in particular locations such as the inner curvature of LA1, LA2 (approximately 1–2  $L/D$  downstream) where it remained close to 20  $\text{dyn}/\text{cm}^2$ . The inner surface is also the site of the highest OSI that was relatively unchanged with exercise (e.g.; LA1/LA2 sites where it remained  $>0.15$ ), indicating that these areas may be continually exposed to potentially deleterious indices of WSS that are not mitigated by the submaximal exercise levels tested in our study. These behaviors may result from flow separation on the inner surface at the DA where helical flow changes orientation (Kilner et al. 1993; LaDisa et al. 2011a). In the branches, TAWSS is low and OSI is high on the anterior side at rest and all levels of exercise, indicating that this region may also remain at risk of neointimal thickening despite the overall positive effects of submaximal exercise. Thus the current study allows for quantification of indices of WSS at multiple exercise levels at a local level that is difficult to obtain via imaging alone. This approach indicates which portions of the TA may be at continued risk despite the known cardiovascular benefits of exercise.

### 4.3 Oxygen extraction and NDS

The current results are comparable to those of Calbet et al. (2007) during upright cycling. Their results indicated  $\text{CexO}_2$  in the legs almost doubled from rest to 40 W, with a 25 % increase from 0 W (unloaded pedaling) to 40 W alone. Extraction in the arms rose slightly from rest to 0 W and increased minimally to 40 W effort. However,  $\text{CexO}_2$  for head and trunk together increase as well. Rao et al. (2009) found renal tissue saturation to decrease (equivalent to  $\text{CexO}_2$  decrease) and cerebral saturation to remain steady in the early phase of a treadmill test to exhaustion. These differences may be related to their upright body positioning compared to the supine position used here. Pedaling while supine puts all tissues at the same level as the heart and therefore may enhance blood flow to cerebral and renal vascular beds in excess of oxygen demand, thus increasing tissue oxygen saturation and decreasing  $\text{CexO}_2$  (Ide et al. 1999). While our results show a linear decrease in  $\text{CexO}_2$  with exercise in the non-exercising renal and cerebral tissues, leg  $\text{CexO}_2$  increased the most from rest to  $\text{HR}_{130}$  then appear to stabilize. This could be due to a lag between oxygen delivery and utilization followed by adaption to exercise, or possibly extraction being more similar between exercise levels. In contrast, shoulder  $\text{CexO}_2$  is relatively constant up to  $\text{HR}_{130}$  then rises at higher levels,

possibly due to global sympathetic response of increased cardiac output with minimal utilization in the arm or more tensing of arm muscle with increased exercise. When combined with our TAWSS results reviewed above, the  $\text{CexO}_2$  results further indicate that the effects of submaximal exercise at the levels tested in this study may be similar enough between levels to preclude the need for all three levels in future experiments, but suggest that an exercise level closer to exhaustion may

The other objective of this study was to determine relationships between  $\text{CexO}_2$  and BF indices that may be used in a predictive manner in future studies. The clearest of these is the linear relationship seen between the change in LCCA flow distribution and cerebral  $\text{CexO}_2$ . Since the common carotid arteries feed only the cerebral vasculature, a non-exercising tissue bed, this trend is not surprising. The change in dAo flow distribution was linearly related to leg  $\text{CexO}_2$  but the relationship would likely be stronger if BF to other major vascular beds could be accounted for. A linear decrease in renal blood flow with heart rate was quantified by Sidhu et al. (2011) and observed with PC-MRI by Taylor et al. (2002) at heart rates similar to those in this study. Those results could be used to predict blood flow to the kidneys, allowing for direct comparison to the kidney  $\text{CexO}_2$  calculations and improving the estimate of dAo blood flow and its relationship to leg tissue  $\text{StO}_2$ . In contrast, the relationship between changes in LSA flow and  $\text{CexO}_2$  was surprisingly weak. This could be due to intermittent tensing of the shoulder and forearms which would restrict flow and increase oxygen demand. The competing effects of vasoconstriction instigated by the sympathetic nervous system and local vasodilation of the skeletal muscle to promote blood flow during tensing may also play a role.

### 4.4 Limitations

The current findings should be interpreted within the constraints of several potential limitations. Choosing exercise levels based on HR normalizes for subject fitness level, but is more difficult to keep constant compared to prescribed workloads. One alternative would be to create subject-specific workloads prior to experimentation, which would require more sophisticated methods of ascertaining subject fitness. Nonetheless, HR levels remained steady enough for flow acquisition. It has also been suggested that because the upright posture for exercise is more indicative of natural motion, it is of greater merit for assessing exercise-induced hemodynamics (Cheng et al. 2004). Hemodynamic parameters differ between upright and supine positions due to the effects of gravity (Braden and Carroll 1999; Hsia et al. 2000), but supine exercise stress testing has also been shown to be viable for achieving high levels of cardiovascular perfor-

mance necessary for analysis at lower workloads and heart rates (Dagianti et al. 1998).

Our subjects for this pilot study were volunteers which precluded the use of gadolinium contrast in MR imaging; thus, for the anatomy scan we were limited to using the 3D Navigator sequence which lasts up to 15 min and therefore was not compatible with continuous pedaling for multiple exercise levels. Due to this limitation in the imaging protocol and insufficient data about vessel material properties, the geometric model for each subject was the same for rest and each of the three exercise levels and rigid walls were assumed for all models. The assumed rigidity likely overestimates WSS values at rest. As the level of exercise increases, distention at higher loading causes the aorta to stiffen but also change its geometry in ways not captured by the models.

The computed outlet boundary conditions use the pulse pressure method which is rooted in the relationship between pressure, flow and resistance. In this method the mean flow measured for each outlet via PC-MRI is matched with simulated mean flow within some acceptable range of error (e.g.; typically 5%). Since the CFD simulation must satisfy conservation of mass, flow distributions among the model outlets were set by subtracting the mean flow in each of the upstream branches from the inlet flow and assuming the remainder of flow proceeds through the dAo. However, the computed mean values from the PC-MRI data may not seem to satisfy conservation of mass when calculated since a number of vessels present in vivo that receive flow are not adequately resolved by the imaging data, and the computational version of the TA does not include several branches such as the intercostal arteries that are known to take 7–12% of flow in this region.

The cumulative percentage distributions shown in Fig. 5 indicate that some subjects (e.g. subject 1) experienced consistent shifts toward higher values of TAWSS in the head and neck arteries with exercise that are likely favorable, while other subjects had redistribution of values that might be concerning. Changes in TAWSS for the head and neck arteries during exercise are modest relative to those in the dAo and likely depend largely on the extent to which these arteries could be modeled before the degradation of imaging data, which also varied among subjects in this study.

This investigation was designed in part to show the feasibility of TA BF acquisition during exercise in a study of healthy young adults. Despite the small sample size ( $n = 6$ ), this research provides feasibility data for a novel exercise MRI protocol in conjunction with CFD modeling. The current window of time required for MRI data acquisition limited the number of exercise levels that could be attained before subject exhaustion to three. The resulting small number of time points (in this case, 4) is not enough to consider possible nonlinear relationships between CexO<sub>2</sub> and FD, though we concede that these may exist and could be further revealed if data at more exercise levels were available. Nonetheless,

these data may be used to design a powered prospective study to gather normative data for a new larger cohort of healthy subjects and later extend to subjects with disease. Currently, the experimental protocol has been applied to persons of adult size, whose torso length allows PC-MRI of vasculature not too far from the magnet isocenter. The current exercise protocol may need modification for individuals of shorter stature (i.e. children).

#### 4.5 Future work

The following steps comprise a preliminary procedure for using NIRS CexO<sub>2</sub> data as surrogates for exercise MRI-derived BF data to create subject-specific boundary conditions for CFD modeling based on the results presented here. Consistent with our stated objectives, ensemble-averaged waveforms for rest and each exercise level are also provided in an online repository ([www.datadryad.org](http://www.datadryad.org)). This procedure could also be modified pending results from future studies that may better estimate shoulder, renal, and dAo BF or CexO<sub>2</sub> as surmised above.

1. Perform cardiac MRI to acquire morphology and resting BF in the AAo, IA, LCA, and LSA.
2. Use ensemble-averaged PC-MRI waveforms to create inflow waveform contours for each exercise level by scaling to subject-specific exercise CO predicted as 130, 150, and 170% of resting CO as discerned from the linear relationship with change in HR.
3. Perform (non MRI) supine pedaling protocol with NIRS to obtain BP and regional tissue StO<sub>2</sub> and calculate CexO<sub>2</sub>.
4. Predict FD and mean BF for LCCA and dAo using the linear relationships with cerebral and leg CexO<sub>2</sub> found with regression.
5. Estimate LSA BF from its diameter and AAo flow (Zamir et al. 1992).
6. Estimate three-element Windkessel parameters using the pulse pressure method (Stergiopoulos et al. 1994, 1999) with the mean BF determined in steps 4 and 5 as well as measured BP values.

## 5 Conclusions

Understanding hemodynamics during exercise may be of particular interest in patients with congenital and acquired heart disease. For instance, for those post-repair of aortic coarctation, as long-term morbidity is only partially explained by residual arch stenosis and is thought instead to result from vascular abnormalities that manifest differently in pre- and post-coarctation vascular beds (Celermajer and Greaves 2002; LaDisa et al. 2011a). Exercise testing for these patients

is currently used to assess indices such as arm-leg BP gradients (Trojnaraska et al. 2007) under stress conditions. An exercise MRI protocol, such as that developed here, could supplement currently available cardiac MRI functional data by providing regional flow quantification during exercise that may lead to increased understanding of hemodynamic vascular changes seen in patients with cardiovascular disease. The addition of exercise flow data to CFD modeling will help depict local changes in indices of WSS experienced during exercise, which is more reflective of real-life situations for patients (LaDisa et al. 2011a; Wentzel et al. 2005). These local TAWSS and OSI indices have the potential to contribute to pathology and addressing them may alter disease progression (Liu et al. 2015).

In conclusion, the current results indicate that O<sub>2</sub> extraction values calculated from NIRS measurements during exercise have the potential to be used to estimate BF (reflective of PC-MRI-derived flow measurements) in the TA and the brachiocephalic arteries. Use of real-time exercise NIRS

data to estimate flow will expand the utility of CFD modeling to aid in patient diagnosis, management, and treatment. We are optimistic that the current results will have a future role in investigating exercise-induced cardiovascular alterations in a variety of diseases of the TA and may become standard of care in the future.

**Acknowledgments** This work was supported by an American Heart Association Postdoctoral Fellowship, 10POST4210030 (to LE) and a National Institutes of Health Award R15HL096096-01 (to JFL). We also gratefully acknowledge the guidance and contributions of Mary Krolkowski RN, MSN, Kristen Andersen, Sheila Moore MD FACR, Robert Prost PhD, Barbara Hilker, Marjorie Bisette, Jim Joers PhD, David Wendell PhD, Brett Arand MS, Timothy Gundert MS, Nutta-On Promjunyakul PhD, and Atefeh Razavi MS.

## Appendix

See Table 4

**Table 4** Preprocess and 3D segmentation parameters used in ITK-Snap to reconstruct geometrically representative computer models of the thoracic aorta and its head and neck branches

| Subject           | Preprocess method | Preprocess parameters |               |              | Segmentation parameters |           |           | Number of iterations |
|-------------------|-------------------|-----------------------|---------------|--------------|-------------------------|-----------|-----------|----------------------|
|                   |                   | Gaussian blurring     | Edge contrast | Edge mapping | Balloon                 | Curvature | Advection |                      |
| <i>Aorta</i>      |                   |                       |               |              |                         |           |           |                      |
| 1                 | Image edges       | 2.0                   | 0.1           | 2.0          | 1.5                     | 0.3       | 5.0       | 30                   |
| 2                 | Image edges       | 1.5                   | 0.18          | 3.0          | 1.5                     | 0.3       | 5.0       | 30                   |
| 3                 | Image edges       | 2.0                   | 0.2           | 3.0          | 1.5                     | 0.3       | 5.0       | 30                   |
| <i>Thresholds</i> |                   |                       |               |              |                         |           |           |                      |
| 4                 | Intensity regions | 836–2508              |               |              | 1.0                     | 0.5       | N/A       | 30                   |
| 5                 | Intensity regions | 770–2502              |               |              | 1.0                     | 0.5       | N/A       | 20                   |
| 6, Top            | Intensity regions | 677–1806              |               |              | 1.0                     | 0.5       | N/A       | 30                   |
| 6, Bottom         | Intensity regions | 445–1831              |               |              | 1.0                     | 0.5       | NA        | 20                   |
| <i>Branches</i>   |                   |                       |               |              |                         |           |           |                      |
| 1                 | Image edges       | 2.0                   | 0.1           | 2.0          | 1.5                     | 2.0       | 5.0       | 25                   |
| 2                 | Image edges       | 1.0                   | 0.2           | 2.0          | 1.0                     | 0.2       | 2.0       | 25                   |
| 3                 | Image edges       | 2.0                   | 0.1           | 2.0          | 1.0                     | 0.2       | 5.0       | 30                   |
| 4                 | Image edges       | 1.0                   | 0.1           | 2.0          | 1.0                     | 0.5       | 2.0       | 15                   |
| 5                 | Image edges       | 0.5                   | 0.2           | 2.0          | 1.0                     | 0.5       | 2.0       | 15                   |
| 6                 | Image edges       | 1.0                   | 0.1           | 2.0          | 1.0                     | 0.5       | 2.0       | 20                   |

## References

- Antiga L, Piccinelli M, Botti L, Ene-Iordache B, Remuzzi A, Steinman DA (2008) An image-based modeling framework for patient-specific computational hemodynamics. *Med Biol Eng Comput* 46:1097–1112. doi:10.1007/s11517-008-0420-1
- Baris RR, Israel AL, Amory DW, Benni P (1995) Regional cerebral oxygenation during cardiopulmonary bypass. *Perfusion* 10:245–248
- Berens RJ et al (2006) Near infrared spectroscopy monitoring during pediatric aortic coarctation repair. *Paediatr Anaesth* 16:777–781. doi:10.1111/j.1460-9592.2006.01956.x
- Blanco PJ, Trenhago PR, Fernandes LG, Feijoo RA (2012) On the integration of the baroreflex control mechanism in a heterogeneous model of the cardiovascular system. *Int J Numer Methods Biomed Eng* 28:412–433. doi:10.1002/cnm.1474
- Boron WF, Boulpaep EL (eds) (2005) *Medical physiology*, 2nd edn. Elsevier Inc, Philadelphia
- Braden DS, Carroll JF (1999) Normative cardiovascular responses to exercise in children. *Pediatr Cardiol* 20:4–10 discussion 11
- Calbet JA, Gonzalez-Alonso J, Helge JW, Sondergaard H, Munch-Andersen T, Boushel R, Saltin B (2007) Cardiac output and leg and arm blood flow during incremental exercise to exhaustion on the cycle ergometer. *J Appl Physiol* 103:969–978
- Celermajer DS, Greaves K (2002) Survivors of coarctation repair: fixed but not cured. *Heart* 88:113–114
- Chakravarti S, Srivastava S, Mitnacht AJ (2008) Near infrared spectroscopy (NIRS) in children. *Semin Cardiothorac Vasc Anesth* 12:70–79. doi:10.1177/1089253208316444
- Chatzis AC et al (2008) Mid-term results following surgical treatment of congenital cardiac malformations in adults. *Cardiol Young* 18:461–466. doi:10.1017/S1047951108002576
- Cheng CP, Herfkens RJ, Lightner AL, Taylor CA, Feinstein JA (2004) Blood flow conditions in the proximal pulmonary arteries and vena cavae: healthy children during upright cycling exercise. *Am J Physiol Heart Circ Physiol* 287:H921–926. doi:10.1152/ajpheart.00022.2004
- Cheng CP, Schwandt DF, Topp EL, Anderson JH, Herfkens RJ, Taylor CA (2003) Dynamic exercise imaging with an MR-compatible stationary cycle within the general electric open magnet. *Magn Reson Med* 49:581–585. doi:10.1002/mrm.10364
- Covidien INVOS 5100C Cerebral/Somatic Oximeter (2009). <http://www.covidien.com/rms/products/cerebral-somatic-oximetry/invos-5100c-cerebral-somatic-oximeter>
- Dagianti A, Penco M, Bandiera A, Sgorbini L, Fedele F (1998) Clinical application of exercise stress echocardiography: Supine bicycle or treadmill? *Am J Cardiol* 81:62G–67G
- Denis R, Perrey S (2006) Influence of posture on pulmonary O<sub>2</sub> uptake kinetics, muscle deoxygenation and myoelectrical activity during heavy-intensity exercise. *J Sports Sci Med* 5:254–265
- Dillon-Murphy D, Noorani A, Nordsletten D, Figueroa CA (2015) Multi-modality image-based computational analysis of haemodynamics in aortic dissection. *Biomech Model Mechanobiol*. doi:10.1007/s10237-015-0729-2
- Faggiano E, Antiga L, Puppini G, Quarteroni A, Luciani GB, Vergara C (2013) Helical flows and asymmetry of blood jet in dilated ascending aorta with normally functioning bicuspid valve. *Biomech Model Mechanobiol* 12:801–813. doi:10.1007/s10237-012-0444-1
- Frydrychowicz A et al (2008) Multidirectional flow analysis by cardiovascular magnetic resonance in aneurysm development following repair of aortic coarctation. *J Cardiovasc Magn Reson* 10:30. doi:10.1186/1532-429X-10-30
- Frydrychowicz A et al (2009) Three-dimensional analysis of segmental wall shear stress in the aorta by flow-sensitive four-dimensional-MRI. *J Magn Reson Imaging* 30:77–84. doi:10.1002/jmri.21790
- Ganong WF (2005) *Review of medical physiology*, 22nd edn. McGraw-Hill, New York
- Gonzalez-Alonso J, Mortensen SP, Dawson EA, Secher NH, Damsgaard R (2006) Erythrocytes and the regulation of human skeletal muscle blood flow and oxygen delivery: role of erythrocyte count and oxygenation state of haemoglobin. *J Physiol* 572:295–305. doi:10.1113/jphysiol.2005.101121
- Gonzalez-Alonso J, Richardson RS, Saltin B (2001) Exercising skeletal muscle blood flow in humans responds to reduction in arterial oxyhaemoglobin, but not to altered free oxygen. *J Physiol* 530:331–341
- Grassi B, Pogliaghi S, Rampichini S, Quaresima V, Ferrari M, Marconi C, Cerretelli P (2003) Muscle oxygenation and pulmonary gas exchange kinetics during cycling exercise on-transitions in humans. *J Appl Physiol* 95:149–158. doi:10.1152/jappphysiol.00695.2002
- Green D, Cheatham C, Reed C, Dembo L, O'Driscoll G (2002) Assessment of brachial artery blood flow across the cardiac cycle: retrograde flows during cycle ergometry. *J Appl Physiol* 93:361–368
- Hansen J, Sander M, Hald CF, Victor RG, Thomas GD (2000) Metabolic modulation of sympathetic vasoconstriction in human skeletal muscle: role of tissue hypoxia. *J Physiol Lond* 527:387–396. doi:10.1111/j.1469-7793.2000.00387.x
- Heiberg E, Sjögren J, Ugander M, Carlsson M, Engblom H, Arheden H (2010) Design and validation of segment-freely available software for cardiovascular image analysis. *BMC Med Imaging* 10:1. doi:10.1186/1471-2342-10-1
- Hoffman GM et al (2004) Changes in cerebral and somatic oxygenation during stage 1 palliation of hypoplastic left heart syndrome using continuous regional cerebral perfusion. *J Thorac Cardiovasc Surg* 127:223–233. doi:10.1016/j.jtcvs.2003.08.021
- Hsia TY, Khambadkone S, Redington AN, Migliavacca F, Deanfield JE, de Leval MR (2000) Effects of respiration and gravity on infradiaphragmatic venous flow in normal and Fontan patients. *Circulation* 102:148–153
- Ide K, Horn A, Secher NH (1999) Cerebral metabolic response to submaximal exercise. *J Appl Physiol* 87:1604–1608
- Kautz SA, Brown DA (1998) Relationships between timing of muscle excitation and impaired motor performance during cyclical lower extremity movement in post-stroke hemiplegia. *Brain* 121(Pt 3):515–526
- Kilner PJ, Yang GZ, Mohiaddin RH, Firmin DN, Longmore DB (1993) Helical and retrograde secondary flow patterns in the aortic arch studied by three-directional magnetic resonance velocity mapping. *Circulation* 88:2235–2247
- Kim HJ, Figueroa CA, Hughes TJR, Jansen KE, Taylor CA (2009) Augmented Lagrangian method for constraining the shape of velocity profiles at outlet boundaries for three-dimensional finite element simulations of blood flow. *Comput Method Appl Mech Eng* 198:3551–3566. doi:10.1016/j.cma.2009.02.012
- Kim HJ, Jansen KE, Taylor CA (2010) Incorporating autoregulatory mechanisms of the cardiovascular system in three-dimensional finite element models of arterial blood flow. *Ann Biomed Eng* 38:2314–2330. doi:10.1007/s10439-010-9992-7
- Kim HJ, Vignon-Clementel IE, Figueroa CA, LaDisa JF, Jansen KE, Feinstein JA, Taylor CA (2009b) On coupling a lumped parameter heart model and a three-dimensional finite element aorta model. *Ann Biomed Eng* 37:2153–2169. doi:10.1007/s10439-009-9760-8

- Kurth CD, Uher B (1997) Cerebral hemoglobin and optical pathlength influence near-infrared spectroscopy measurement of cerebral oxygen saturation. *Anesth Analg* 84:1297–1305
- Kwon S, Feinstein JA, Dholakia RJ, LaDisa JF Jr (2014) Quantification of local hemodynamic alterations caused by virtual implantation of three commercially available stents for the treatment of aortic coarctation. *Pediatr Cardiol* 35:732–740. doi:10.1007/s00246-013-0845-7
- LaDisa JF et al (2011a) Computational simulations for aortic coarctation: representative results from a sampling of patients. *J Biomech Eng* 133:091008. doi:10.1115/1.4004996
- LaDisa JF et al (2011) Computational simulations demonstrate altered wall shear stress in aortic coarctation patients treated by resection with end-to-end anastomosis. *Congenit Heart Dis* 6:432–443. doi:10.1111/j.1747-0803.2011.00553.x
- Ladisa JF Jr, Taylor CA, Feinstein JA (2010) Aortic oarctation: recent developments in experimental and computational methods to assess treatments for this simple condition. *Prog Pediatr Cardiol* 30:45–49. doi:10.1016/j.ppedcard.2010.09.006
- Lau KD, Figueroa CA (2015) Simulation of short-term pressure regulation during the tilt test in a coupled 3D–0D closed-loop model of the circulation. *Biomech Model Mechanobiol* 14:915–929. doi:10.1007/s10237-014-0645-x
- Les AS et al (2010) Quantification of hemodynamics in abdominal aortic aneurysms during rest and exercise using magnetic resonance imaging and computational fluid dynamics. *Ann Biomed Eng* 38:1288–1313. doi:10.1007/s10439-010-9949-x
- Liu X, Sun A, Fan Y, Deng X (2015) Physiological significance of helical flow in the arterial system and its potential clinical applications. *Ann Biomed Eng* 43:3–15. doi:10.1007/s10439-014-1097-2
- Loomba RS, Danduran ME, Dixon JE, Rao RP (2014) Effect of Fontan fenestration on regional venous oxygen saturation during exercise: further insights into Fontan fenestration closure. *Pediatr Cardiol* 35:514–520. doi:10.1007/s00246-013-0817-y
- Macdonald J, Forouzan O, Warczytowa J, Wieben O, Francois CJ, Chesler NC (2015) MRI assessment of aortic flow and pulse wave velocity in response to exercise. *J Cardiovasc Magn Reson* 17:M2–M2. doi:10.1186/1532-429X-17-S1-M2
- MacPhee SL, Shoemaker JK, Paterson DH, Kowalchuk JM (2005) Kinetics of O<sub>2</sub> uptake, leg blood flow, and muscle deoxygenation are slowed in the upper compared with lower region of the moderate-intensity exercise domain. *J Appl Physiol* 99:1822–1834. doi:10.1152/jappphysiol.01183.2004
- Malek AM, Alper SL, Izumo S (1999) Hemodynamic shear stress and its role in atherosclerosis. *JAMA* 282:2035–2042
- Markl M et al (2003) Generalized reconstruction of phase contrast MRI: analysis and correction of the effect of gradient field distortions. *Magn Reson Med* 50:791–801. doi:10.1002/mrm.10582
- Mehta JP, Verber MD, Wieser JA, Schmit BD, Schindler-Ivens SM (2009) A novel technique for examining human brain activity associated with pedaling using fMRI. *J Neurosci Methods* 179:230–239. doi:10.1016/j.jneumeth.2009.01.029
- Moireau P, Xiao N, Astorino M, Figueroa CA, Chapelle D, Taylor CA, Gerbeau JF (2012) External tissue support and fluid-structure simulation in blood flows. *Biomech Model Mechanobiol* 11:1–18. doi:10.1007/s10237-011-0289-z
- Mosteller RD (1987) Simplified calculation of body-surface area. *N Engl J Med* 317:1098. doi:10.1056/NEJM198710223171717
- Muller J, Sahni O, Li X, Jansen KE, Shephard MS, Taylor CA (2005) Anisotropic adaptive finite element method for modelling blood flow. *Comput Methods Biomech Biomed Engin* 8:295–305
- Niezen RA, Doornbos J, van der Wall EE, de Roos A (1998) Measurement of aortic and pulmonary flow with MRI at rest and during physical exercise. *J Comput Assist Tomogr* 22:194–201
- Pedersen EM, Kozerke S, Ringgaard S, Scheidegger MB, Boesiger P (1999) Quantitative abdominal aortic flow measurements at controlled levels of ergometer exercise. *Magn Reson Imaging* 17:489–494. doi:S0730725X98002094 [pii]
- Peeters JM, Bos C, Bakker CJ (2005) Analysis and correction of gradient nonlinearity and B0 inhomogeneity related scaling errors in two-dimensional phase contrast flow measurements. *Magn Reson Med* 53:126–133. doi:10.1002/mrm.20309
- Poliner LR, Dehmer GJ, Lewis SE, Parkey RW, Blomqvist CG, Willerson JT (1980) Left ventricular performance in normal subjects: a comparison of the responses to exercise in the upright and supine positions. *Circulation* 62:528–534
- Rao RP et al (2009) Measurement of regional tissue bed venous weighted oximetric trends during exercise by near infrared spectroscopy. *Pediatr Cardiol* 30:465–471. doi:10.1007/s00246-009-9393-6
- Rao RP, Danduran MJ, Loomba RS, Dixon JE, Hoffman GM (2012) Near-infrared spectroscopic monitoring during cardiopulmonary exercise testing detects anaerobic threshold. *Pediatr Cardiol* 33:791–796. doi:10.1007/s00246-012-0217-8
- Sahni O, Muller J, Jansen KE, Shephard MS, Taylor CA (2006) Efficient anisotropic adaptive discretization of the cardiovascular system. *Comput Methods Biomech Biomed Eng* 195:5634–5655
- Sampath S, Derbyshire JA, Ledesma-Carbayo MJ, McVeigh ER (2011) Imaging left ventricular tissue mechanics and hemodynamics during supine bicycle exercise using a combined tagging and phase-contrast MRI pulse sequence. *Magn Reson Med* 65:51–59. doi:10.1002/mrm.22668
- Samyn MM et al (2015) Cardiovascular magnetic resonance imaging-based computational fluid dynamics/fluid-structure interaction pilot study to detect early vascular changes in pediatric patients with type 1 diabetes. *Pediatr Cardiol* 36:851–861. doi:10.1007/s00246-014-1071-7
- Sidhu P, Peng HT, Cheung B, Edginton A (2011) Simulation of differential drug pharmacokinetics under heat and exercise stress using a physiologically based pharmacokinetic modeling approach. *Can J Physiol Pharmacol* 89:365–382. doi:10.1139/y11-030
- Steeden JA, Atkinson D, Taylor AM, Muthurangu V (2010) Assessing vascular response to exercise using a combination of real-time spiral phase contrast MR and noninvasive blood pressure measurements. *J Magn Reson Imaging* 31:997–1003. doi:10.1002/jmri.22105
- Stergiopoulos N, Meister JJ, Westerhof N (1994) Simple and accurate way for estimating total and segmental arterial compliance: the pulse pressure method. *Ann Biomed Eng* 22:392–397
- Stergiopoulos N, Segers P, Westerhof N (1999) Use of pulse pressure method for estimating total arterial compliance in vivo. *Am J Physiol Heart Circ Physiol* 276:H424–428
- Tanaka H, Shimizu S, Ohmori F, Muraoka Y, Kumagai M, Yoshizawa M, Kagaya A (2006) Increases in blood flow and shear stress to nonworking limbs during incremental exercise. *Med Sci Sports Exerc* 38:81–85
- Tang BT, Cheng CP, Draney MT, Wilson NM, Tsao PS, Herfkens RJ, Taylor CA (2006) Abdominal aortic hemodynamics in young healthy adults at rest and during lower limb exercise: quantification using image-based computer modeling. *Am J Physiol Heart Circ Physiol* 291:H668–676
- Taylor CA, Cheng CP, Espinosa LA, Tang BT, Parker D, Herfkens RJ (2002) In vivo quantification of blood flow and wall shear stress in the human abdominal aorta during lower limb exercise. *Ann Biomed Eng* 30:402–408
- Thomas SN, Schroeder T, Secher NH, Mitchell JH (1989) Cerebral blood flow during submaximal and maximal dynamic exercise in humans. *J Appl Physiol* 67:744–748
- Trojnarska O et al (2007) Cardiopulmonary exercise test in the evaluation of exercise capacity, arterial hypertension, and degree of descending aorta stenosis in adults after repair of coarctation of the aorta. *Cardiol J* 14:76–82

- Varjavand N (2000) The Interactive Oxyhemoglobin Dissociation Curve (2011). <http://www.ventworld.com/resources/oxydisso/dissoc.html>
- Vignon-Clementel IE, Figueroa CA, Jansen KE, Taylor CA (2006) Outflow boundary conditions for three-dimensional finite element modeling of blood flow and pressure in arteries. *Comput Methods Appl Mech Eng* 195:3776–3796
- Voight ML, Hoogenboom BT, Prentice WE (2007) *Musculoskeletal interventions: techniques for therapeutic exercise*. McGraw-Hill, New York
- Weber TF, von Tengg-Kobligh H, Kopp-Schneider A, Ley-Zaporozhan J, Kauczor HU, Ley S (2011) High-resolution phase-contrast MRI of aortic and pulmonary blood flow during rest and physical exercise using a MRI compatible bicycle ergometer. *Eur J Radiol* 80:103–108. doi:10.1016/j.ejrad.2010.06.045
- Wendell DC et al (2013) Including aortic valve morphology in computational fluid dynamics simulations: initial findings and application to aortic coarctation. *Med Eng Phys* 35:723–735. doi:10.1016/j.medengphy.2012.07.015
- Wentzel JJ et al (2005) Does shear stress modulate both plaque progression and regression in the thoracic aorta? Human study using serial magnetic resonance imaging. *J Am Coll Cardiol* 45:846–854. doi:10.1016/j.jacc.2004.12.026
- Westerhof N, Stergiopulos N, Noble MIM (2005) *Snapshots of hemodynamics: an aid for clinical research and graduate education*. Springer, New York
- Yushkevich PA, Piven J, Hazlett HC, Smith RG, Ho S, Gee JC, Gerig G (2006) User-guided 3D active contour segmentation of anatomical structures: significantly improved efficiency and reliability. *NeuroImage* 31:1116–1128. doi:10.1016/j.neuroimage.2006.01.015
- Zamir M, Sinclair P, Wonnacott TH (1992) Relation between diameter and flow in major branches of the arch of the aorta. *J Biomech* 25:1303–1310
- Zanjani KS et al (2008) Feasibility and efficacy of stent redilatation in aortic coarctation. *Catheter Cardiovasc Interv* 72:552–556. doi:10.1002/ccd.21701